


SYNTHESIZING DATA PRODUCTS, MATHEMATICAL MODELS, AND OBSERVATIONAL MEASUREMENTS FOR LAKE TEMPERATURE FORECASTING

BY MAIKE F. HOLTHUIJZEN^{1,a} , ROBERT B. GRAMACY^{2,b} CAYELAN C. CAREY^{3,c}
DAVID M. HIGDON^{4,d} AND R. QUINN THOMAS^{5,e}

¹Sandia National Labs Dept 8738, ^amholthuijzen@alumni.uidaho.edu

²Department of Statistics, Virginia Tech, ^brbg@vt.edu

³Department of Biological Sciences, Virginia Tech, ^ccayelan@vt.edu

⁴Department of Statistics, Virginia Tech, ^ddhigdon@vt.edu

⁵Departments of Forest Resources & Environmental Conservation and Biological Sciences, Virginia Tech, ^erqthomas@vt.edu

We present a novel forecasting framework for lake water temperature profiles, crucial for managing lake ecosystems and drinking water resources. The General Lake Model (GLM), a one-dimensional process-based model, has been widely used for this purpose, but, similar to many process-based simulation models, it: requires a large number of input variables, many of which are stochastic; presents challenges for uncertainty quantification (UQ); and can exhibit model bias. To address these issues, we propose a Gaussian process (GP) surrogate-based forecasting approach that efficiently handles large, high-dimensional data and accounts for input-dependent variability and systematic GLM bias. We validate the proposed approach and compare it with other forecasting methods, including a climatological model and raw GLM simulations. Our results demonstrate that our bias-corrected GP surrogate (GPBC) can outperform competing approaches in terms of forecast accuracy and UQ up to two weeks into the future.

1. Introduction. Process-based models are critical for understanding, managing, and forecasting environmental phenomena and are widely used in ecological research. The use of process-based models for one application in particular, the forecasting of lake water temperature profiles, is crucial for policies and decisions that impact the health of aquatic ecosystems (Carey et al., 2022; Cuddington et al., 2013). A lake temperature profile refers to the variation in water temperature at different depths within a lake. In aquatic ecosystems, water quality and the health of aquatic organisms is strongly associated with water temperature (Carey et al., 2022), which influences various biological processes, such as the growth and distribution of aquatic flora and fauna (Wetzel, 2001). Warmer water temperatures can lead to accelerated growth of harmful phytoplankton, which can produce toxins that threaten aquatic and human health (Carey et al., 2012). Lake temperature forecasts that extend at least 30 days into the future, include uncertainty quantification (UQ), and are updated frequently are crucial to adequately managing drinking water resources, mitigating water quality degradation, and planning for the health of lake ecosystems (Thomas et al., 2023; Carey et al., 2022). In this study, we focus on forecasting lake temperatures at ten depths at Falling Creek Reservoir (FCR), a small drinking water reservoir located in Vinton, Virginia, USA (Figure 1 left).

There are several approaches for forecasting lake temperatures (Lofton et al., 2023), the most simple of which are climatological forecasts. These are based on historical data, capturing broader trends, and are accurate at long (15+ day) horizons (Thomas et al., 2023). Such

Keywords and phrases: surrogate modeling, Gaussian process, Vecchia approximation, stochastic kriging.

forecasts for FCR can be constructed using data collected by in situ water temperature sensors (denoted by the red dot in Figure 1 left). By definition, climatological forecasts do not vary substantively year upon year, predictive limits do not vary with the forecast horizon, and they lack sharpness (the tendency of a model to predict outside of the mean Gneiting, Balabdaoui and Raftery, 2007), reducing their value for near-term water quality management.

Improved lake temperatures forecasts can be obtained by driving a process-based lake ecosystem model with an ensemble of weather forecasts (Cho et al., 2020; Thomas et al., 2020, 2023). Lake ecosystem models are designed to simulate heat transfer within aquatic ecosystems (Mooij et al., 2010) and can encompass a wide range of processes, including hydrodynamics (Hipsey et al., 2019), water quality (Hipsey et al., 2012; Cole and Wells, 2021), nutrient cycling (Janse, Aldenberg and Kramer, 1992), and ecological interactions (Leon et al., 2006). One such model, the one-dimensional (1D) General Lake Model (GLM; Hipsey et al., 2019)¹ is a general-purpose lake ecosystem model that can simulate thermal dynamics in a vertical column of a water body. GLM takes into account the physical characteristics of the lake, such as its depth, surface area, and geometry, water inputs from surrounding areas, and external factors (e.g., meteorology) to simulate water movement, mixing, and circulation patterns within a column (Hipsey et al., 2019). GLM has been used to forecast long-term lake ecosystem responses to climate change by driving it with climate projections (Christianson, Johnson and Hooten, 2020; Gal et al., 2020; Fenocchi et al., 2018). It has also been used to study the effects of climate change on long-term historical lake dynamics (Ladwig et al., 2018; Shikhani et al., 2022) as well as to research general historical lake hydrodynamics (Huang et al., 2017; Bueche, Hamilton and Vetter, 2017) and water quality indicators (Ladwig et al., 2021; Ward et al., 2020).

However, GLM has characteristics that make it challenging to use for near-term (1-30 days into the future) forecasts of lake temperatures. To obtain lake temperature forecasts, GLM must be driven with forecasted weather products. Furthermore, since GLM is a deterministic model, UQ associated with forecasts can only be derived if it is driven with an *ensemble* of weather forecasts or parameter values, although we do not consider the latter here. Importantly, like all process-based models, GLM is a simplified version of reality that does not perfectly represent processes that govern energy transfer within a water column, let alone in an entire (three-dimensional) lake. Any systematic biases, or other errors that result from such oversimplifications, need to be accounted for.

Observations provide a critical foundation for assessing the accuracy and reliability of GLM. At FCR, water temperature sensors installed at 10 depths (surface to 9m depth by 1m increments) have collected a rich and continuous observational data record starting in July 2018 (red dot in Figure 1, left). One can get a sense of GLM performance for the FCR study region by comparing GLM output to sensor data. Figure 1 (right) shows an example of GLM simulations (yellow) and sensor observations (black) at 6m depth (a depth near the thermocline where model performance is often lowest relative to other depths) as well as a *surrogate model* for GLM in blue (discussed momentarily). These GLM simulations exhibit a pronounced warm bias between April and October with respect to observations. Although the bias appears obvious via a visual comparison of raw GLM output and observations, it is not possible to visually separate GLM bias from observational noise. To do so, an additional model for the bias itself is necessary, and we expand upon this idea in the following sections.

Our contributions. We seek accurate 1-30 day ahead ensemble forecasts of lake temperatures at 10 depths at FCR with well-calibrated UQ. These forecasts are made by

¹The authors apologize for this overloaded acronym; throughout “GLM” refers to the General Lake Model, not a generalized linear model.

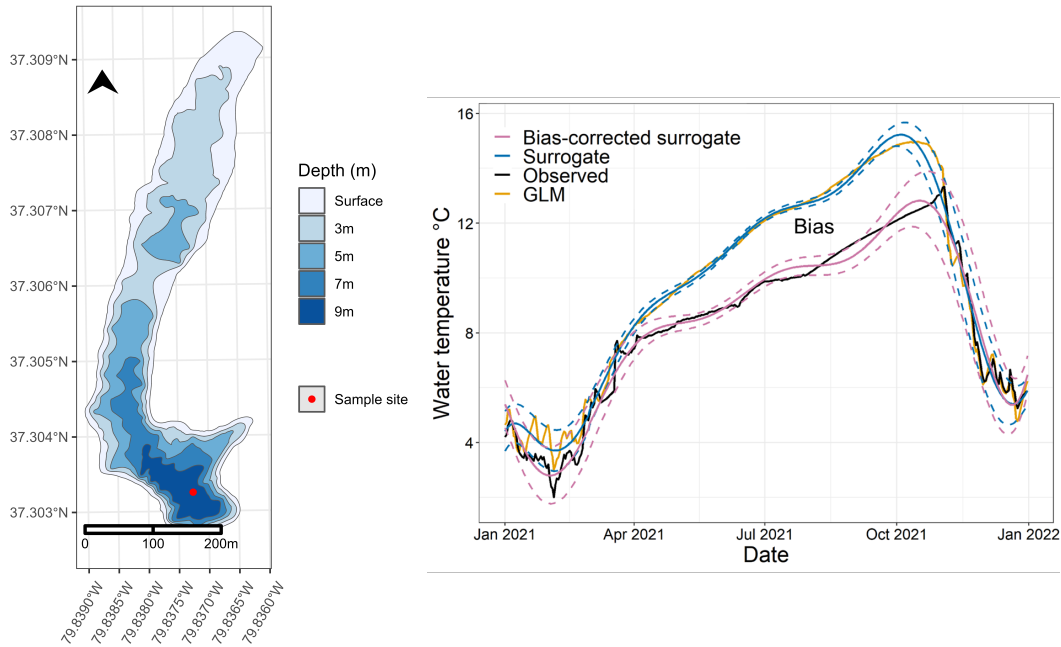


FIG 1. Left: *Falling Creek Reservoir (FCR) in Vinton, Virginia, USA (37.30°N, 79.84°W)*. The location of sensors, installed in 2018, are denoted by the red dot on the map and are located at 10 depths (surface to 9m at 1-m increments). Lake depth (m) is shown by the blue color scale. Right: Example GLM simulations (yellow) and observations (black) for 2021 at a lake depth of 6m. Means and 90% prediction intervals of a GLM surrogate are shown in blue; a bias-corrected version is shown in pink.

driving GLM with a 31-member ensemble of weather forecasts generated by the National Oceanic and Atmospheric Administration Global Ensemble Forecast System (NOAA-GEFS; Hamill et al., 2022, see <https://www.ncei.noaa.gov/products/weather-climate-models/global-ensemble-forecast>). Construction of ensemble lake temperature forecasts is facilitated with automated code (available at https://github.com/maikeh7/Surrogate_Assisted_GLM) and is inspired by Thomas et al. (2020). Figure 2 diagrams how NOAA ensemble forecasts and data from FCR are used to construct lake temperature forecasts with GLM.

Examples of NOAA-driven GLM forecasts (hereafter “NOAA-GLM”) at FCR for 1–30 days in the future are shown in Figure 3. At lower horizons, the forecasts of individual ensemble members are similar, but as horizon increases, forecasts diverge. There is considerable variability in within reference dates: forecasts starting on 2020-10-30 (fall, Figure 3A) are less variable compared to forecasts originating on 2021-01-01 (winter, Figure 3B). Variability also differs according to lake depth, where shallow depths exhibit more variation than deeper ones. While simple, this approach is useful: forecasts have long (30-day) horizons, and uncertainty can be derived from variability among ensemble members. However, it does not account for GLM bias, and uncertainty is not modeled directly, making UQ less reliable.

A more robust alternative to generating lake temperature forecasts involves building a *probabilistic* representation of NOAA-GLM, which could subsequently improve prediction accuracy and UQ, while also denoising the 31 ensemble forecast trajectories. This approach could accommodate functional forms of bias, allowing for a flexible bias-correction. Modeling bias is also advantageous because it allows the bias to be separated from observational noise (Liu et al., 2009); as we saw in Figure 1 (right), this is not possible using raw model output and observations. Observe in Figure 1 how one type of statistical model (blue lines) adequately smooths GLM simulations while providing appropriate UQ. While the blue lines

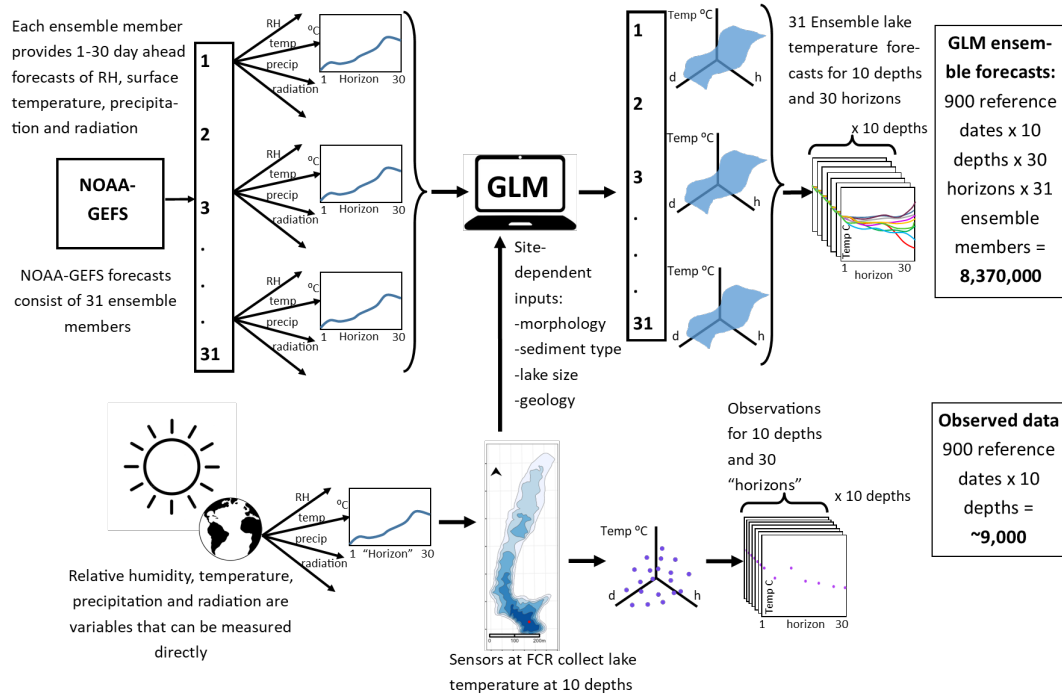


FIG 2. This schematic shows how NOAA forecasts and data from FCR are utilized to generate 1–30 day ahead forecasts at 10 depths for the time period of interest (2020-10-03 and 2023-06-10). NOAA 1–30 day ahead forecasts consist of 31 ensemble members of 4 variables: precipitation, relative humidity, surface temperature, and solar radiation. Temperature sensors at FCR (red dot) collect data at 10 depths (surface to 9m depth at 1-m intervals). To generate lake temperature forecasts for FCR for the 900 reference dates in 2020-10-03 and 2023-06-10, GLM requires weather forecast inputs as well as site-dependent features such as lake size, area, sediment type, and general morphology. Given the weather inputs and site-dependent parameters from FCR, GLM can generate 31, 1 to 30 day-ahead forecasts of lake temperatures at 10 depths. Each of the 31 resulting forecasts can be visualized as a 2D surfaces of lake temperature over horizon (h) and depth (d). Observed data from FCR can be visualized as 2D scatter plots of lake temperature over h and d . It is important to note that the amount of observed data is substantially lower than those generated by GLM.

represent a statistical model for only a single GLM realization, we propose to extend this idea to modeling GLM ensemble forecast trajectories. Figure 1 (right) also shows the mean and 90% prediction intervals resulting from a *bias-corrected* model (pink lines). In contrast to the biased model (blue) fitted to GLM simulations, the mean of the bias-corrected model provides a very good approximation to observations, and UQ is reliable.

One way to statistically model NOAA-GLM forecasts is through the use of a computer model *surrogate*. A surrogate emulates the *behavior* of a computer model such as GLM but does so without the model’s physical equations in its implementation (Santner et al., 2018). Gaussian process (GP) surrogates are the canonical choice as they have many desirable properties, including flexibility, smoothness, predictive accuracy, and reliable UQ (Gramacy, 2020; Williams and Rasmussen, 2006). Model bias can also be modeled with a GP (Kennedy and O’Hagan, 2001; Liu et al., 2009), allowing for robust and versatile bias-correction. One major challenge to using a GP surrogate is the decomposition bottleneck of multivariate normal (MVN) covariance matrices. In GP fitting/prediction, these matrices are sized commensurately with the square of the training data of size n , incurring a decomposition cost that is cubic in n flops. In our application, n is very large. Each of the 31 NOAA ensemble members results in 31 NOAA-GLM forecasts for 30 horizons and 10 lake depths, producing a total dataset size of: 900 reference dates \times 30 horizons \times 10 depths \times 31 en-

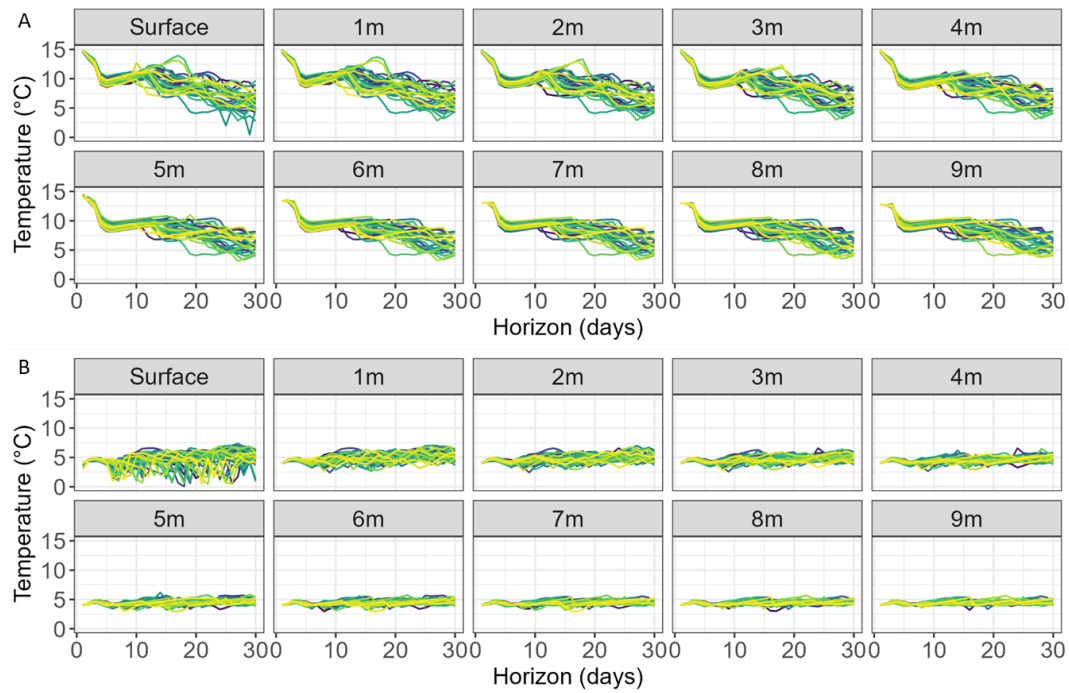


FIG 3. NOAA-GLM lake temperature forecasts ($^{\circ}\text{C}$) for FCR. Forecasts start on reference dates A) 2020-10-30 and B) 2021-01-01. Colors of lines denote trajectories of individual ensemble members. Panel numbers denote lake depth (m).

semble members = 8,370,000, a formidable data size for any model-fitting enterprise, and especially so for GP surrogates.

GP surrogates have been used in hydrological (Razavi, Tolson and Burn, 2012) and environmental applications (Fer et al., 2018), model calibration (Fer et al., 2018), sensitivity (Oakley and O’Hagan, 2004) and uncertainty analysis (Yang et al., 2018; Roy et al., 2018). However, *bias-corrected*, GP surrogates that can handle input-dependent variability and big data have never been implemented in the context of ecological forecasting. The main contribution of this paper is the development of a novel lake temperature forecasting workflow for water quality management, where NOAA-GLM forecasts are represented by a bias-corrected GP surrogate. Importantly, our approach, which can generate forecasts at 10 depths and 30 forecast horizons, is efficient enough to allow for *iterative* forecasting, where forecasts, models and datasets are updated daily.

This paper is organized as follows: we begin with a review of GP surrogates for computer models and follow with a detailed description of the forecasting workflow and the statistical techniques associated with it. We validate our proposed framework and show how forecasts from our framework compare to one in which bias is not corrected, raw GLM output, and a climatological forecast. We then discuss results and provide concluding remarks.

2. Background and proof-of-concept. Our forecasting framework operates on the frontier of Gaussian process (GP) surrogate modeling (e.g., Gramacy, 2020) for synthesizing computer model output, observations, and correcting bias. A basic GP setup is introduced here, building upon Figure 1. That earlier analysis comprises a proof-of-concept, suggesting that forecasts utilizing GLM and lake temperatures measured by sensors would benefit from meta-modeling and bias correction. Ultimately, we will need a higher-powered strategy in order to cope with a large corpus of NOAA-GLM runs, which is the subject of Section 3.

2.1. *Gaussian process surrogate modeling.* GPs are popular as surrogates for computer model simulation experiments (e.g., Santner et al., 2018), and more widely as a nonlinear and nonparametric regression tool (e.g., Williams and Rasmussen, 2006), because they furnish accurate predictors with appropriate coverage when used to model smooth and stationary (i.e., physical) phenomena. Here we utilize GPs in both contexts: for computer model simulations and on observational data. As models for computer experiments, GP surrogates can be crucial to enabling subsequent tasks such as optimization, calibration, and sensitivity analysis (e.g., Gramacy, 2020). One advantage GPs enjoy over other nonlinear regression choices – such as splines (Friedman, 1991), polynomial regression (Jones, 2001), and neural networks (Farfán and Cea, 2021) – is well-calibrated, probabilistic uncertainty quantification (UQ), which is easy to filter to the “subsequent tasks” listed above. This UQ extends to input-dependent variability (e.g., Ankenman, Nelson and Staum, 2008; Binois, Gramacy and Ludkovski, 2018), such as is seen in GLM forecasts over increasing horizon [Figure 3] and is discussed in greater detail below in Section 3.

Consider a computer model M represented as a function $f : \mathbb{R}^p \rightarrow \mathbb{R}$ that maps inputs to outputs, whose pairs over n_M runs of a simulation campaign comprise data $D_{n_M} = (\mathbf{x}_i, y_i)$, $i = 1 \dots n_M$. Let $\mathbf{X}_{n_M} = (\mathbf{x}_1^\top, \mathbf{x}_2^\top, \dots, \mathbf{x}_{n_M}^\top) \in \mathbb{R}^{n_M \times p}$, collect inputs, and $\mathbf{Y}_{n_M}^M = (y_1, y_2, \dots, y_{n_M})^\top$ outputs. Utilizing a GP model, or *prior*, for f amounts to specifying that outputs $\mathbf{Y}_{n_M}^M$ jointly follow a multivariate normal distribution (MVN). In a GP regression context it is common that the MVN be specified with a mean of zero, and a covariance Σ that is determined by (inverse) distances between inputs \mathbf{X}_{n_M} :

$$(1) \quad \mathbf{Y}_{n_M}^M \sim \mathcal{N}_{n_M}(\mathbf{0}_{n_M}, \Sigma(\mathbf{X}_{n_M})) \quad \text{where, e.g.,} \quad \Sigma^{ij} = \tau^2(k(q(\mathbf{x}_i, \mathbf{x}_j)) + g\mathbb{I}_{\{i=j\}}).$$

There are many choices for the form of $\Sigma(\mathbf{X}_{n_M})$. Most are similar to Eq. (1). A *kernel* $k(\cdot)$ performs the inversion, like $k(q) = e^{-q}$, and $q(\cdot, \cdot)$ calculates a (scaled) Euclidean distance:

$$(2) \quad q(\mathbf{x}_i, \mathbf{x}_j) = \sum_{\ell=1}^p \left(\frac{\|x_{i,\ell} - x_{j,\ell}\|^2}{\gamma_\ell} \right)^{1/2}.$$

Our setup is largely indifferent to variations in choices of q , k , etc. In our empirical work we use the q specified in Eq. (2), and the Matern kernel k with smoothness level fixed at 3.5.

In what follows we express the setup in Eq. (1) concisely as $\mathcal{GP}(D_{n_M})$, given a choice of $k(\cdot)$, distance $q(\cdot)$ and hyperparameters $\boldsymbol{\theta} = (\boldsymbol{\gamma}, g, \tau^2)$. The $\boldsymbol{\gamma} = (\gamma_1, \gamma_2, \dots, \gamma_d)$ are so-called *lengthscale* or *range* parameters, where $1/\gamma_\ell$ determines the “relevance” of the x_ℓ input (e.g., Liu et al., 2019). The overall amplitude of the response is determined by *scale* parameter τ^2 , and the *nugget* g operates as a dial partitioning that amplitude between signal (τ^2) and noise ($\tau^2 g$). Observe that g is only augmenting the diagonal of Σ , implementing an independent and constant (i.e., homoskedastic) noise component, an aspect which we relax in Section 3.

Ideally, settings for hyperparameters are learned from data. The GP model (1) for $\mathbf{Y}_{n_M}^M$ gives rise to a likelihood through the density of an MVN:

$$(3) \quad L(\boldsymbol{\theta}; D_{n_M}) \propto |\Sigma_{\boldsymbol{\theta}}|^{-1/2} \exp \left(-\frac{1}{2} (\mathbf{Y}_{n_M}^M)^\top \Sigma_{\boldsymbol{\theta}}^{-1} \mathbf{Y}_{n_M}^M \right)$$

which can be used to learn settings $\hat{\boldsymbol{\theta}}_{n_M}$; see, e.g., Gramacy (2020, Chapter 5). Observe that $\boldsymbol{\theta}$ is buried in $\Sigma_{\boldsymbol{\theta}}$, although we often drop the subscript to streamline the notation. It is common in the literature to presume that settings $\hat{\boldsymbol{\theta}}_{n_M}$ have already been estimated given data D_{n_M} and focus analysis on other aspects of inference. More detail on the nuances of our own estimation procedures for an expanded hyperparameter $\boldsymbol{\theta}$ is provided in Section 3. However, it is worth pointing out that determinants and inverses, as required to evaluate the likelihood (3) require cubic in n_M flops for dense matrices $\Sigma_{\boldsymbol{\theta}}$, a computational bottleneck for large n_M .

Training data sizes in the low thousands is manageable; tens of thousands require minutes or hours, or are entirely infeasible.

One of the most important uses for GPs involves prediction. When modeling computer simulations, the predictive equations are what are referred to as the “surrogate”, because these $\hat{f}(\cdot)$ may be used in lieu of a new simulation $f(\cdot)$. In geostatistics these are sometimes called the *kriging equations* (Banerjee, Carlin and Gelfand, 2003). Suppose we wish to predict \mathbf{Y}_{n_M} at a new $n' \times d$ set of input configurations collected in the rows of \mathcal{X} . Deriving the distribution for $\mathbf{Y}(\mathcal{X})$ involves stacking the MVN for \mathbf{Y}_{n_M} together with an analogous one for $\mathbf{Y}(\mathcal{X})$, i.e., where the latter follows Eq. (1) but where $\Sigma(\mathcal{X})$ is used instead. The joint, $(n_M + n')$ -dimensional MVN has a covariance structure with block diagonal components $\Sigma(\mathbf{X}_{n_M})$ and $\Sigma(\mathcal{X})$, and off-diagonal $\Sigma(\mathbf{X}_{n_M}, \mathcal{X})$ and its transpose. The quantity $\Sigma(\mathbf{X}_{n_M}, \mathcal{X})$ is derived from (inverse) distances between training \mathbf{X}_{n_M} and testing \mathcal{X} but involves no nugget (g) augmentation. Then, using MVN conditioning identities, we may derive the predictive/conditional distribution $\mathbf{Y}(\mathcal{X}) \mid D_{n_M} \sim \mathcal{N}_{n'}(\mu_{n_M}(\mathcal{X}), \Sigma_{n_M}(\mathcal{X}))$, where

$$(4) \quad \mu_{n_M}(\mathcal{X}) = k(\mathbf{X}_{n_M}, \mathcal{X})^\top (k(\mathbf{X}_{n_M}) + g\mathbb{I}_{n_M})^{-1} \mathbf{Y}_{n_M},$$

and $\Sigma_{n_M}(\mathcal{X}) = \hat{\tau}^2 (k(\mathcal{X}) + g\mathbb{I}_{n'}) - k(\mathbf{X}_{n_M}, \mathcal{X})^\top (k(\mathbf{X}_{n_M}) + g\mathbb{I}_{n_M})^{-1} k(\mathbf{X}_{n_M}, \mathcal{X}).$

Modulo $\hat{\theta}$, these equations provide full predictive uncertainty. Any intervals derived from the quantiles of the covariance diagonal could be considered predictive intervals (PIs).

If, instead, one is interested in predictions for $f(\mathcal{X}) = \mathbb{E}\{\mathbf{Y}(\mathcal{X})\}$ one would take $g = 0$ in $k(\mathcal{X}) + g\mathbb{I}_{n'}$ in Eq. (4) to obtain confidence intervals (CIs) instead. More specifically, and since we will need to use it later, if $\boldsymbol{\mu}_{n_M} \equiv \mu_{n_M}(\mathcal{X}) = \mathbb{E}\{\mathbf{Y}_{n_M}(\mathcal{X})\}$, then

$$(5) \quad \text{Var}\{\boldsymbol{\mu}_{n_M}\} = \hat{\tau}^2 (k(\mathcal{X}) - k(\mathbf{X}_{n_M}, \mathcal{X})^\top (k(\mathbf{X}_{n_M}) + g\mathbb{I}_{n_M})^{-1} k(\mathbf{X}_{n_M}, \mathcal{X})).$$

Note that $\text{Var}\{\boldsymbol{\mu}_{n_M}\} < \Sigma_{n_M}(\mathcal{X})$, uniformly over all entries of those matrices.² Moreover $\text{Var}\{\boldsymbol{\mu}_{n_M}\} \rightarrow \mathbf{0}$ as $n_M \rightarrow \infty$ as long as \mathbf{X}_{n_M} fills out the input space. In other words, we can learn to emulate f with the surrogate \hat{f} perfectly with enough data. We provide a compare and contrast of PIs and CIs in Figure 6, alongside a description of heteroskedastic modeling in Section 3.2. Finally, it is again worth noting the cubic cost of matrix inversion implied in Eqs. (4–5) above, even after conditioning on θ .

2.2. Gaussian process surrogates for lake temperatures. To provide an illustration, and to outline how we intend to use GPs for modeling lake temperatures, consider the following setup. Take f/M as GLM and run it for each day of 2021, driven by actual/observed environmental variables in that year, and extract temperatures for ten depths: surface/0 to 9m. So, using the notation established above, \mathbf{Y}_{n_M} is comprised of $n_M = 366 \times 10 = 3660$ simulation outputs, and \mathbf{X}_{n_M} has $p = 2$ columns indexing time t in Julian day, and depth d , in meters, respectively. Figure 1 (right) shows a “slice” of *some* of the elements of this data (D_{n_M}) as a yellow line where $\mathbf{X}_{n_M}[\cdot, 2] = 6$ meters. (The full D_{n_M} is ten times bigger.)

Now consider modeling D_{n_M} as a GP, i.e., $\mathcal{GP}(D_{n_M})$. Specifically, estimate hyperparameters ($\theta = (\gamma, g, \tau^2)$) by MLE (3), and plug these values $\hat{\theta}$ into predictive equations (4) using $\mathcal{X} = \mathbf{X}_{n_M}$, i.e., to evaluate the surrogate at the training locations. Such n_M , in the the small tens of thousands, is on the cusp of manageable with modern architectures and specialized linear algebra libraries such as Intel MKL in about an hour. The left panel of Figure 4 shows the resulting surrogate mean surface $\mu_{n_M}(\mathcal{X})$ over depth (m) and day of year. This corresponds to the solid blue lines in the right panel of Figure 1 (right), which provide a slice

²Note also that a non-zero nugget g is present elsewhere in Eq. (5), and when modeling deterministic simulations there is no difference between PIs and CIs.

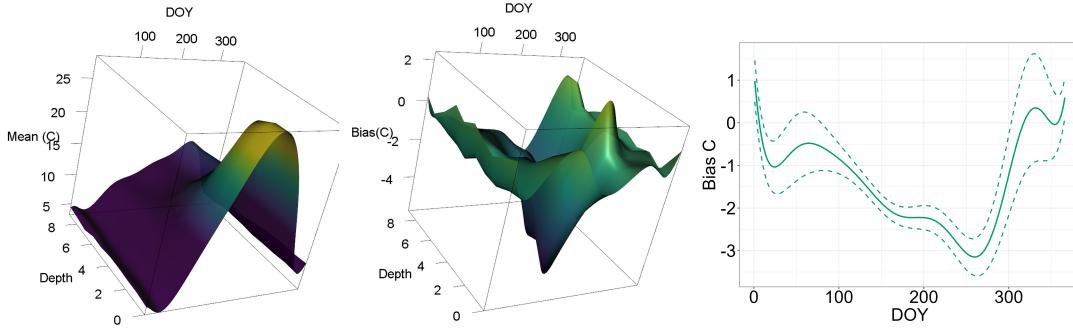


FIG 4. The left panel shows the GLM surrogate mean surface $\mu_{n_M}(\mathcal{X})$ over day of year (DOY) and depth (m) for 2021. The middle panel shows the mean surface $\mu_b(\mathcal{X})$ of the bias GP $\hat{b}(\cdot)$. The right panel shows a 1D slice of $\mu_b(\mathcal{X})$ where the second column of $\mathcal{X}[:, \cdot] = 6$ meters, along with 90% PIs corresponding to the slice of $\mathcal{X}[:, 2] = 6$. For predictions $\hat{f}(\mathcal{X})$ (left) and $\hat{b}(\mathcal{X})$ (middle and right), $\mathcal{X} \equiv \mathbf{X}_{n_m}$.

at 6m ($\mathcal{X}[:, 2] = 6$) along with 90% PIs corresponding (only) to the slice of $\mathcal{X}[:, 2] = 6$ meters. Observe in Figure 1 (right) how the surrogate smooths over the GLM simulations and that the intervals have appropriate coverage.

Predictions from the surrogate $\hat{f}(\mathcal{X})$ in Figures 1 (right) and 4 (left) are not “forecasts” because they do not correspond to the future. These predictions are derived from known/measured environmental variables, that, for forecasting, would be unknown/require additional modeling. That is the subject of Section 3. However, such a setup could easily be extended to serve as a surrogate for a “climatology”, if data were GLM simulations driven by observed environmental variables over a period of several years. The data setup would be the same, with two inputs and one output, but with much larger n_M . We do not illustrate that here, but we do compare to a similar model later in our empirical work in Section 5.

Importantly, $\hat{f}(\mathcal{X})$ in Figures 1–4 allow us to abstract the raw GLM simulations by smoothing over the noise/jitters that come from noisy or chaotic measurements of environmental variables. Like any statistical model, the surrogate helps us separate signal from noise. Once we have the signal, we can compare it to something else, like actual physical/sensor measurements of lake temperature (black line in Figure 1). From Figure 1, it is obvious that, during the period from April to November, GLM is biased in this application. The surrogate is not essential to make that observation, because the signal and the magnitude of the bias are both high. However, the narrow PIs here provide evidence of a strong bias signal.

The surrogate is more useful in the colder months, when it provides an adequate approximation to observations. Observe that the black lines go outside the blue-dashed PIs in early 2021. This means that, during this period, GLM likely has a warm bias, a signal that would have been hard to separate from noise without the surrogate – in particular without good UQ. Meanwhile, in late 2021, the situation is different: GLM is likely unbiased; any differences with sensor measurements are probably due to noise.

These are qualitative assessments that can be made concrete and quantitative, by using the surrogate to estimate the bias as a function of time and depth. Once estimated, a model for the bias can be used to make a correction (i.e., to obtain a “bias-corrected surrogate”). Let $\mathbf{Y}_{n_F}^F$ denote the n_F -length vector of sensor observations, or *field data*, at FCR. In our example, $n_F = n_M$ since we have observed temperatures on the same days and at the same depths as our GLM simulations ($\mathbf{X}_{n_F} = \mathbf{X}_{n_M}$). We could easily have more simulations than sensor observations, say, and we will later in Section 3.

Let $\mu_{n_m} \equiv \mu(\mathbf{X}_{n_F})$, following Eq. (4) with $\mathcal{X} = \mathbf{X}_{n_F}$, which in this case is equivalent to using $\mathcal{X} = \mathbf{X}_{n_M}$ (though it need not be). Using this quantity, we may measure the bias of our

GLM surrogate relative to the sensor measurements as

$$(6) \quad \mathbf{Y}_{n_F}^b = \mathbf{Y}_{n_F}^F - \boldsymbol{\mu}_{n_M}.$$

We may then form a data set of observed discrepancies between model and field data $D_{n_F}^b = (\mathbf{X}_{n_F}, \mathbf{Y}_{n_F}^b)$. Then, regarding bias, or bias correction, $b(\cdot)$ as an unknown function like $f(\cdot)$, we may model it as $\mathcal{GP}(D_{n_F}^b)$ and infer it’s hyperparameters, etc. Readers familiar with the computer modeling literature will recognize a similarity between this setup and the so-called Kennedy and O’Hagan framework (KOH; [Kennedy and O’Hagan, 2001](#)) where the two processes: computer model M and field data F are meta-modeled jointly, without directly calculating discrepancies. Our setup here is more modular ([Liu et al., 2009](#)), and thus more amenable to up-scaling as described in Section 3. Also, crucially, we are not learning any so-called calibration parameters, although we may explore that in future work (Section 6), so there is no potential for confounding between bias correction and surrogate modeling fits (e.g., [Brynjarsdóttir and O’Hagan, 2014](#)).

Predictions obtained via Eq. (4), with moments we shall denote as $\mu_{n_F}^b(\mathcal{X})$ and $\Sigma_{n_F}^b(\mathcal{X})$, evaluated at $\mathcal{X} \equiv \mathbf{X}_{n_m}$ forming $\hat{b}(\cdot)$ via $\mathcal{GP}(D_{n_F}^b)$, are shown in the middle and right panels of Figure 4. The middle panel shows the full predictive mean surface $\mu_{n_F}^b(\mathcal{X})$ over depth and DOY, while the right panel shows only the 6m depth slice with 90% PIs. Note that $\mu_{n_F}^b(\mathcal{X})$ is much more “wiggly” than the surface in the left panel. Focusing on the 6m slice in the right panel of Figure 4, observe the following: in early 2021, the mean predicted bias is small in magnitude and are close to, but do not always contain zero. This indicates a small (and possibly statistically insignificant) warm bias for GLM during this period. Mid-year the magnitude of the predicted bias is large and negative with narrow PIs, indicating substantial warm bias. Finally, later in the year there is a zero/non-significant bias.

Now consider Figure 1 (*right*), which shows the bias correction, in pink, formed as the sum of two GP fits: GLM surrogate \hat{f} and bias correction \hat{b} . One may think of this as (a slice through) the sum of the first two panels in Figure 4, but that would only account for means. A more accurate depiction would involve 2d versions of the slices through the full distribution(s) summarized by the blue lines (\hat{f}) in Figure 1 (*right*) and for the bias correction \hat{b} in the right panel of Figure 4. Mathematically, since \hat{f} and \hat{b} are both MVNs we can follow formulas for sums of MVNs which involve summing the means ($\mu_{n_M}(\mathcal{X}) + \mu_{n_F}^b(\mathcal{X})$) and covariances ($\text{Var}\{\mu_{n_M}(\mathcal{X})\} + \Sigma_{n_F}^b(\mathcal{X})$) and subtracting off cross-covariances. The pink lines shown in Figure 1 omits subtracted cross-covariances, somewhat overestimating uncertainty.

It is important to note that we are not using $\Sigma_{n_M}(\mathcal{X})$, the full predictive variance for $Y(\mathcal{X} | D_{n_M})$ from Eq. (4) for the bias corrected (co-) variance. Instead we are using the nugget-free one (5) because only the estimated GLM surrogate mean $\boldsymbol{\mu}_{n_M}$ was used to define the observed discrepancies, not actual GLM simulations. We shall delve into this further in Section 3.2, and offer a visual in Figure 6 comparing CIs and PIs. For more details, see [Gramacy \(2020, Sections 5.3.2 & 8.1.3\)](#). Observe from Figure 1 (*right*) that the resulting predictions and PIs in pink are accurate and provide good coverage for the field data. This is perhaps not surprising as we are effectively predicting in-sample, and the GP (or two GPs in fact) provide in a highly flexible non-linear regression. It is their performance out of sample, in particular, as a forecaster for future lake temperatures, which is our focus.

Although we turn to forecasting next in Section 3, it is worth noting that an analysis such as this is valuable in its own right. Through this exercise, we have gained valuable insight into the nature of the bias in GLM model evaluations that resulted in modifications to the GLM version and configuration. This reduced some of the bias, but not all. In what follows, and especially with our empirical validation in Section 3.3, we utilized that new setup.

3. GP surrogates for forecasting. There are two challenges to extending the proof-of-concept in Section 2. The first is conceptual: pivoting the modeling framework toward forecasts. We wish to synthesize computer model runs driven by an ensemble of “plausible futures” provided by another computer model, so that they may be compared to what actually happened, as observed in the field. Specifically in the context of lake temperatures, we need a model for how GLM – driven by NOAA ensembles over extended horizons [Figure 3] – relates to temperatures observed by sensors for various depths at FCR.

The second challenge is technological, centering around modeling fidelity and scale. Thirty-day horizons, and 31 NOAA ensemble members forecasting environmental variables, all studied over the course of multiple years (and depths) where observational data has been obtained, represent a very large, and heteroskedastic [Figure 3], simulation campaign. Both, large scale GP modeling (Heaton et al., 2019) and accommodating input-dependent variance for stochastic simulation (Baker et al., 2022), are on the frontier of the current surrogate modeling landscape, as described by recent reviews [cited above]. Those papers outline many choices, most of which are inappropriate in our setting. Here we describe a setup that provides enough flexibility for our NOAA-GLM at FCR while remaining computationally tractable. We are not aware of any examples of where the two (large scale and heteroskedastic GP modeling) have been combined in one application, either generally or in the specific context of forecasting and bias correction. We aim for a practical setup where most of the work is off-loaded to modern libraries so that it is readily extensible to other applications.

3.1. Modeling a forecasting apparatus. Consider a single horizon of h days into the future, like one day ($h = 1$) or one month ($h = 30$). We could deploy the setup in Section 2, except with time “shifted” by $t - h$ and with NOAA-simulated environmental variables. More specifically, given NOAA 1–30 day ahead forecasts for each reference date in the training period, GLM will produce 1–30 day ahead lake temperatures at 10 depths. Since the training period is in the past, these faux-future forecasts are what NOAA calls “hindcasts”.³ We may then compare NOAA-GLM hindcasts to what really happened on that day, as recorded in the field data of observed sensor measurements. In other words, we relate the hindcast from time $t - h$ ahead h days to time $t - h + h \equiv t$.

Figure 3 shows output from GLM for two reference days t , ten depths d and thirty horizons h for 2021. For now, we focus on a single, particular h , which amounts to taking a vertical slice through the panels of that figure yielding 31 simulated temperatures at each depth. Now average those 31 GLM simulations, separately for each depth, to obtain a single y^M -value as output for reference Julian day t and depth d . If this was done for an entire year, we would have the same data setup as in Section 2 – a single model run for each day and depth in the study period – but now we would be relating the past (time $t - h$) to the present (time t) in a forecasting context. The data set $D_{n_M}^{(h)}$ would have identical \mathbf{X}_{n_M} but $\mathbf{Y}_{n_M}^{(h)}$ would be different, as indicated by the (h) superscript. We could then follow Section 2 methods for fitting a GP surrogate $\mathcal{GP}(D_{n_M}^{(h)})$, obtaining $\mu_{n_M}^{(h)}$ and $\mathbf{Y}_{n_F}^{b(h)}$ analogously (comparing the actual measurement at time t to its forecast derived at time $t - h$) and fit $\mathcal{GP}(D_{n_F}^{b(h)})$ to these data to learn a bias correction.

This can be repeated for each horizon h of interest. Such a setup has much to recommend it. It is modular, in that it uses off-the-shelf tools, and it is computationally tractable because each GP is fit to moderately sized training data, keeping the matrix decompositions manageable. But such modeling is inefficient statistically because separate, independent fits do not account for correlations across horizon, which are clearly evident in Figure 3, both in mean

³Hindcasts are forecasts for past environmental variables pretending the future (also in the past) is unknown.

and in variance. Furthermore, UQ will be less accurate, because through averaging the 31 ensemble GLM simulations, variance information is lost. Finally, since t represents Julian day, adjustments are required to accommodate multiple years of data.

Toward a more holistic model, we propose the following. Let \mathbf{X}_{n_M} represent the matrix of inputs as in Section 2, but now augmented with a horizon column indicating h , which we take as $h \in \{1, \dots, h_{\max} = 30\}$, an ensemble member column $e \in \{1, \dots, 31\}$, and a year column λ . The t column would be interpreted as the day the forecast was made; the last day for which observational data (i.e., the truth) is known, i.e., $t - h$ from the description above, re-labeled. Columns e and λ are merely included to index the data, and we shall provide more detail about how these affect modeling momentarily. We may create such a matrix, i.e., beyond the time and depth columns previously contained in \mathbf{X}_{n_M} from Section 2, via Cartesian product: each day and depth pair matched with each horizon, ensemble member and year so that $n_M \leftarrow n_M \times 30 \times 31 \times 3$ compared to the n_M value in Section 2. Each corresponding entry in the output vector Y_{n_M} corresponds to a campaign of NOAA-GLM runs and other configuration inputs.

Continuing to overload notation from Section 2, we have $D_{n_M} = (\mathbf{X}_{n_M}, \mathbf{Y}_{n_M})$, relating the time in which a forecast is made, (t, λ) , to GLM-simulated temperature(s) output at depth d at h horizons into the future, indexed by NOAA ensemble member e . Supposing we could surrogate model these simulations, we could again follow the recipe in Section 2 to use their predictive equations to define discrepancies, learn bias corrections, and filter them through to forecasts. There is some nuance to the last few steps, which we outline in Section 3.4, once the surrogate modeling details are in place. However, while it is easy to say “fit a surrogate to D_{n_M} ”, i.e., $\mathcal{GP}(D_{n_M})$, it is hard to do. These data are huge, with n_M in the millions; moreover, NOAA-GLM simulations (across ensemble members) are heteroskedastic [Figure 3]. Addressing these technological challenges are the subject of the next two subsections.

3.2. Heteroscedastic surrogate modeling. The first way that we make the surrogate modeling enterprise more manageable is to disregard the ensemble column e in \mathbf{X}_{n_M} and thereby treat forecasts from each e as independent conditional on time and depth. This statistical modeling assertion is purely for computational convenience; it is not faithful to the simulation mechanism. While NOAA ensemble members are independent of one another, each realization evolves in a time-dependent manner. Forecasts from the prior day or depth for a specific ensemble member might contain valuable data for predicting the following day or depth for that same member, and potentially others. Nonetheless, our assumption of independence aligns with the essence of ensemble modeling. The 31-member NOAA ensemble allows for the measurement of a variety of environmental conditions, whose variability grows over time. We apply these to GLM simulations, as depicted in Figure 3.

This “modeling hack” means that each of 31 ensemble forecasts may be treated as *replicates*. Baker et al. (2022) explain that replicates bring two kinds of efficiency. One is computational: the number of sufficient statistics are fewer – 31-fold fewer in this instance. The other is statistical: replicates allow a pure glimpse at variance, without needing to first separate signal from noise. This is especially important when noise levels are changing along with the mean, in a potentially nonlinear way, as we have in Figure 3. The most effective methods for modeling such nonlinear heteroskedasticity (e.g., Goldberg, Williams and Bishop, 1997; Ankenman, Nelson and Staum, 2008; Quadrianto et al., 2009; Lázaro-Gredilla and Titsias, 2011; Binois, Gramacy and Ludkovski, 2018) leverage replication. *Stochastic kriging* (SK; Ankenman, Nelson and Staum, 2008), one of the first of these, is ideal for our setting. SK is sometimes criticized for (a) being moment-based (rather than being completely likelihood-based); and (b) for not jointly modeling the mean and variance process(es). These are valid

concerns when the degree of replication is low. [Ankenman, Nelson and Staum \(2008\)](#) recommend at least ten replicates for each otherwise unique input. We have 31. Joint, likelihood-based modeling, as suggested by many of the other references cited above, is better statistically but much more work computationally.

Suppose that simulation outputs \mathbf{Y}_{n_M} correspond to $n \ll n_M$ unique inputs in \mathbf{X}_{n_M} when ignoring the e column. In our case $n = n_M/31$. Let $\bar{\mathbf{X}}_n$ denote the matrix of those unique inputs, again without the e column, so that $\bar{\mathbf{X}}_n$ is $n \times 4$. Now, consider each row $\bar{\mathbf{x}}_i$ of $\bar{\mathbf{X}}_n$, and let $y_j(\bar{\mathbf{x}}_i)$ denote the j^{th} replicate associated with $\bar{\mathbf{x}}_i$ among the n_i replicates in \mathbf{X}_{n_M} . We have that all $n_i = 31$. Then, calculate the first two moments for these replicates as

$$(7) \quad \bar{y}_i = \frac{1}{n_i} \sum_{j=1}^{n_i} y_j(\bar{\mathbf{x}}_i) \quad s_i^2 = \frac{1}{n_i - 1} \sum_{j=1}^{n_i} (y_j(\bar{\mathbf{x}}_i) - \bar{y}_i)^2, \quad \text{for } i = 1, \dots, n.$$

Finally, store these in $\bar{\mathbf{Y}}_n$ and $\bar{\mathbf{S}}_n$, respectively, to line up with the rows of $\bar{\mathbf{X}}_n$. Note that we use a bar on top of $\bar{\mathbf{X}}_n$ not to indicate that any averaging is involved in their calculation, but instead to visually match up with $\bar{\mathbf{Y}}_n$ and $\bar{\mathbf{S}}_n$, which do involve averaging. Also note that we are dropping the M subscripts to streamline the notation here with the understanding that we are only using this on the computer model runs. If the field data also had replicates we could additionally make use of them there, but our sensors record only one measurement per day.

SK involves modeling $\bar{\mathbf{Y}}_n$ and $\bar{\mathbf{S}}_n$ via GPs rather than operating directly on the original D_{n_M} . It turns out that these $2n$ quantities are not sufficient for \mathbf{Y}_{n_M} in the context of prediction, but they are close. [Binois, Gramacy and Ludkovski \(2018\)](#) show that there are $2n + 1$ sufficient statistics. Nevertheless, [Ankenman, Nelson and Staum \(2008\)](#) argue that inference based on these $2n$ quantities is unbiased asymptotically and minimizes mean-squared error.

Suppose we wish to predict \bar{Y} at new inputs \mathcal{X} with a GP. If the degree of replication is uniform, e.g., $n_i = 31$ for all i , then we could simply plug the $\bar{\mathbf{Y}}_n$ values, along with $\bar{\mathbf{X}}_n$, into Eq. (4) after solving for MLE hyperparameters. We can do the same thing for the second moments $\bar{\mathbf{S}}_n$. This is the essence of SK with two caveats: (a) uniform replication is rare, although that is the case for NOAA-GLM; (b) it helps to explicitly link the mean and variance processes when making forecasts. First, fit a GP to $\bar{\mathbf{S}}_n$, often on a transformed scale (e.g., via log or a log/square-root hybrid ([Johnson et al., 2018](#))) in order to respect positivity. Specifically, fit $\mathcal{GP}(D_n^{(v)})$ where $D_n^{(v)} = (\bar{\mathbf{X}}_n, T(\bar{\mathbf{S}}_n))$ via MLE. For $T(\cdot)$ we prefer the square root to model standard deviations, although a logarithm also works well. Then feed the unique training $\bar{\mathbf{X}}_n$ values into the predictive equations (4), i.e., with $\mathcal{X} = \bar{\mathbf{X}}_n$. Let

$$(8) \quad \mathbf{S}_n = \text{Diag}(T^{-1}(\mu^{(v)}(\bar{\mathbf{X}}_n))/\mathbf{n}) \quad \text{where} \quad \mathbf{n} = (n_1, \dots, n_n).$$

Several quantities may require explanation. Predictions $\mu^{(v)}(\bar{\mathbf{X}}_n)$ are transformed back to the original, variance scale. Dividing these by n_i converts these variances into (squared) standard errors. Each raw $\sqrt{s_i^2/n_i}$ from Eq. (7) is a standard error for $\mathbb{E}\{\bar{y}_i\}$, measuring the amount of response information present for each unique input $\bar{\mathbf{x}}_i$. So $T^{-1}(\mu^{(v)}(\bar{\mathbf{x}}_i))/n_i$ is its GP-smoothed analog, borrowing information from nearby standard errors in \mathbf{x} -space. Finally, the diagonal puts these in a matrix representing our otherwise independent (but not identically distributed) structure for noise on the original \mathbf{Y}_{n_M} .

Similarly, obtain predictions at any *new/forecasting* coordinates \mathcal{X} that may be of interest, like for a particular day t and multiple horizons h into the future. These \mathcal{X} 's could represent genuine forecasts, or hindcasts that would be compared later to sensor measurements, which we discuss further in Section 3.4. Let $s(\mathcal{X}) = \text{Diag}(T^{-1}(\mu^{(v)}(\mathcal{X})))$ capture these back-transformed variance predictions – they are the predictive analog of Eq. (8). Using these, and similar quantities described above, the SK equations are

$$(9) \quad \mu_n^{\text{SK}}(\mathcal{X}) = \tau^2 k(\bar{\mathbf{X}}_n, \mathcal{X})^\top (\tau^2 k(\bar{\mathbf{X}}_n) + \mathbf{S}_n)^{-1} \bar{\mathbf{Y}}_n^M$$

$$(10) \quad \Sigma_n^{\text{SK}}(\mathcal{X}) = \tau^2 (k(\mathcal{X}) + s(\mathcal{X})) - \tau^2 k(\bar{\mathbf{X}}_n, \mathcal{X})^\top (\tau^2 k(\bar{\mathbf{X}}_n) + \mathbf{S}_n)^{-1} \tau^2 k(\bar{\mathbf{X}}_n, \mathcal{X}).$$

Observe in Eq. (9) that augmenting the diagonal of $k(\bar{\mathbf{X}}_n)$ with \mathbf{S}_n results in a scaled nugget-like term, by analogy to $\tau^2 g$ in Eq. (4). It facilitates a signal-to-noise trade-off that is unique to each training data element and/or its degree of replication. Having τ^2 implicitly a part of \mathbf{S}_n prevents a cancellation of τ^2 that would otherwise render a predictive mean equation that is free of this quantity. Smoothed (squared) standard errors \mathbf{S}_n naturally downweight large variance/low replication training data. Crucially, it may be shown that $\mu_n^{\text{SK}}(\mathcal{X}) = \mu_{n_M}(\mathcal{X})$ from Eq. (4), identically, i.e., the full n_M -data predictive mean can be recovered from GP smoothing over the replicate-wise $2n$ almost-sufficient statistics, which could represent a huge computational savings when $n \ll n_M$ as amplified by cubic matrix decomposition.

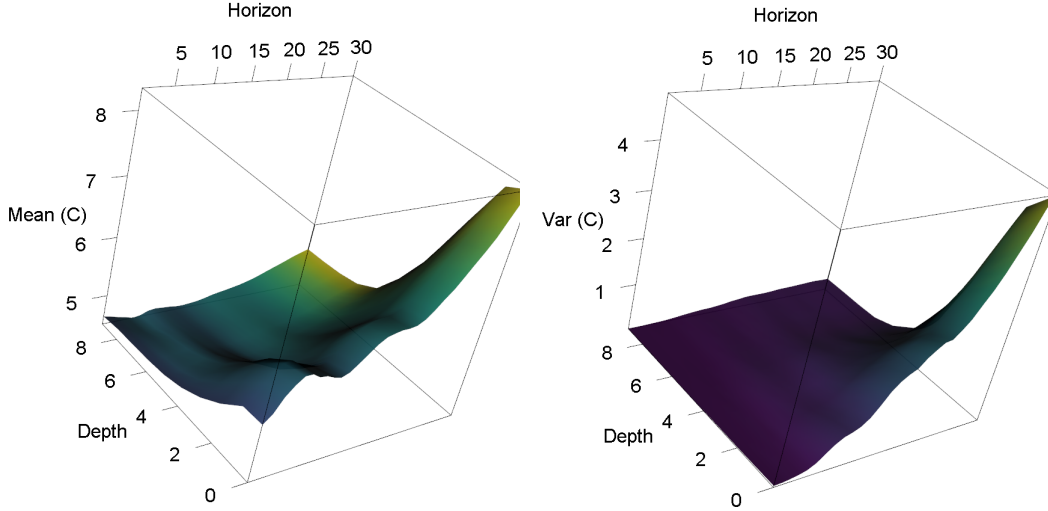


FIG 5. 2d slices of predictive mean $\mu_n^{\text{SK}}(\mathcal{X})$ (left) and variance $\sigma_n^{\text{SK}}(\mathcal{X})^2$ (right) from the (heteroscedastic) GLM surrogate over depth (m) and horizon (days). Together, these summarize a hindcast for 2022-02-19.

To illustrate, consider Figure 5 which is derived from fits of two GPs, for mean and (square root) variance, to a simulation campaign spanning three years over a thirty-day horizon. The data represented in the plot comprises a 2d slice of predictions from those two fits corresponding to a forecast beginning on 2022-02-19, offering a surrogate for the NOAA-GLM hindcast beginning on that date. Focusing first on the left panel, showing $\mu_n^{\text{SK}}(\mathcal{X})$ from Eq. (9), observe that temperature is decreasing with increasing depth, and also generally increasing over horizon, most prominently at the surface (low depths). Both relationships are clearly nonlinear. Now looking at the right panel providing $\sigma_n^{\text{SK}}(\mathcal{X})^2 = \text{Diag}(\Sigma_n^{\text{SK}}(\mathcal{X}))$ we see a similar relationship in the spread of possible temperatures. Variance is much lower at lower depths, even at longer horizons, which makes sense because these depths are more insulated from weather at the surface. At the surface, the variance grows quickly farther out into the future.

Figure 6 shows a 1d slice of the surface(s) in Figure 5 at 1m depth along with additional information. Gray lines indicate raw NOAA-GLM simulations (i.e., a subset of the training data D_{n_M}). Filled purple dots indicate field/sensor observations at 1m depth on the days in question. These latter values are not part of the analysis at this time and are provided for reference only. Of particular note are the dashed orange error-bars indicating a 90% PI derived from $\mu_n^{\text{SK}}(\mathcal{X})$ and $\sigma_n^{\text{SK}}(\mathcal{X})^2$. Observe that the 90% PIs have appropriate coverage. Dotted lines indicate 90% CIs on the mean that are derived by eliminating the $s(\mathcal{X})$ term in Eq. (10), as an analogue to Eq. (5).

It is this squared standard error which is crucial to our bias-correcting analysis described in Section 3.4. Observe that, at least in this view, NOAA-GLM forecasts and their surrogate

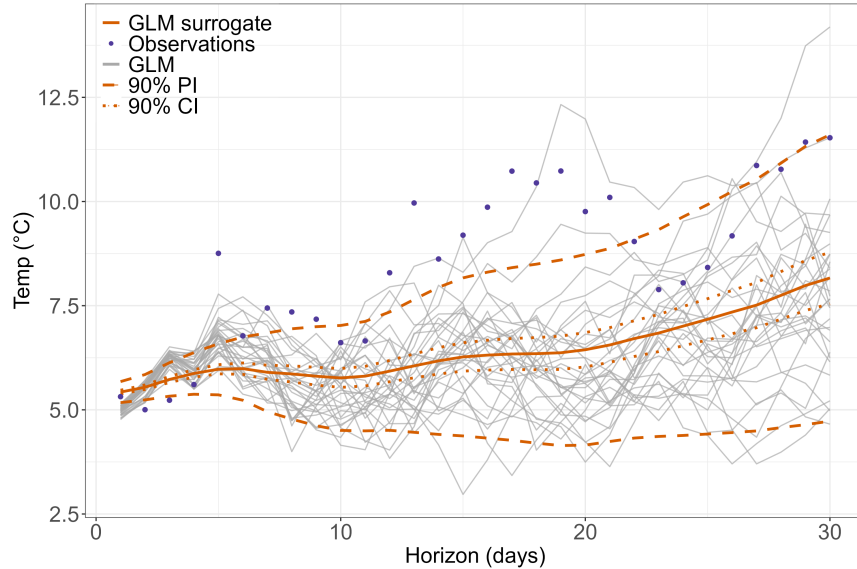


FIG 6. GLM ensemble forecasts 1–30 day-ahead (gray lines) beginning on Feb 10, 2021 along with a 1d slice of the SK surrogate (solid orange line) 90% CIs and PI (dotted and dashed orange lines), respectively.

have a cold bias compared to the field data. But first we must describe how we make these SK calculations with large training data sizes. Although reducing n_M from around 8 million to n around 270,000 (900 reference dates \times 10 depths \times 30 horizons) is helpful, this n is still too large for conventional GP fitting.

3.3. GP surrogates and scalability. The surrogates behind the views in Figures 5 and 6 were constructed using the approximate methods we describe here. Scalable GP approximation has been an active field of late. Techniques include compactly supported kernels (Gneiting, 2002; Kaufman et al., 2011), fixed-rank kriging (Cressie and Johannesson, 2008) inducing points (Banerjee et al., 2008; Quinero-Candela and Rasmussen, 2005; Hensman, Fusi and Lawrence, 2013) local divide-and-conquer (Emery, 2009; Gramacy, 2016) and the Vecchia/nearest-neighbor approximation (Datta et al., 2016; Wu, Pleiss and Cunningham, 2022; Vecchia, 1988; Katzfuss and Guinness, 2021; Guinness, 2018; Zhang and Katzfuss, 2022; Katzfuss et al., 2020; Katzfuss, Guinness and Lawrence, 2022; Katzfuss and Guinness, 2021). We have identified that the so-called scaled Vecchia approximation (SVecchia Katzfuss, Guinness and Lawrence, 2022) is particularly well-suited to our setting, and to surrogate modeling at large because it offers a global model, accommodates input dimension larger than two, allows coordinate-wise lengthscale estimation, and scales in flops that are quasi-linear in training data size, n . Crucially, a user-friendly open-source implementation is provided for R: <https://github.com/katzfuss-group/scaledVecchia>.

The crux of the Vecchia approximation is a simple identity linking joint and conditional distributions. Consider a vector \mathbf{Y}_n of responses, like one filled with \bar{y}_i -values in Section 3.2 above. The joint probability of \mathbf{Y}_n can be factorized as

$$\begin{aligned}
 p(\mathbf{Y}_n) &= p(y_1)p(y_2 | y_1)p(y_3 | y_2, y_1) \dots p(y_n | y_1 \dots y_{n-1}) \\
 (11) \quad &\approx \prod_{i=1}^n p(y_i | y_{c(i)}) \quad \text{where } c(i) \subset \{1, \dots, i-1\},
 \end{aligned}$$

where the second line is an equality if $|c(i)| = i - 1$ and an approximation otherwise. This relationship is true for all $n!$ reordering of the indices. The quality of the approximation depends on the ordering, $|c(i)|$ and the choice of the subset of $\{1, \dots, i - 1\}$ it comprises. Such an approximation is advantageous in particular for GPs, or any MVN-based joint distribution, because the requisite conditionals are available in closed form (4) and the matrices/decompositions are limited by the size of $c(i)$. Taking $|c(i)| = \min(m, i - 1)$, a common simplifying choice, means that each conditional in the product in Eq. (11) requires flops in $\mathcal{O}(m^3)$. If $m \ll n$ this cost represents an enormous computational savings despite that the product involves n of them, i.e., $\mathcal{O}(nm^3)$.

Some additional implementation details make things even faster and allow for distributed computation, which we leave to our references (Stein, Chi and Welty, 2004; Guinness, 2018; Katzfuss and Guinness, 2021; Stroud, Stein and Lysen, 2017; Datta et al., 2016; Wu, Pleiss and Cunningham, 2022; Katzfuss et al., 2020). We have been satisfied with the performance of the defaults offered by the R library linked above, synthesizing many of those elements including composition of the $c(i)$. We settled on $m = 30$ by entertaining an out-of-sample prediction exercise similar to that reported by Sauer, Cooper and Gramacy (2023), which showed diminished returns for larger m -values. Perhaps the most important aspect of that software, compared to other methods based on the Vecchia approximation, is that the effect of an input-dependent lengthscale γ can be learned along with scale τ^2 and (scalar) nugget g via Fisher scoring (Guinness, 2021). The authors call this the ‘‘Scaled Vecchia’’ approximation; however we’ll simply refer to it as Vecchia going forward with the understanding that input-dependent lengthscales are being learned. With this setup we are able to fit GPs with $n \approx 270,000$ as described in Section 3.2 in about twenty seconds on an ordinary workstation (64-bit Intel(R) Core(TM) i9-9900K CPU @ 3.60GHz with 16 cores).

The Vecchia approximation has never been used, and nor to our knowledge has any other large-scale GP approximation, to model input-dependent variances, like through SK (Section 3.2). Fitting second moments $\mathcal{GP}(D_n^{(v)})$ in order to get a predictor for $T(\text{Var}\{Y(\mathcal{X})\})$ is straightforward, because this amounts to feeding in (transformed) s_i -values (7) as responses along with unique inputs \bar{x}_i . The visual in the right panel of Figure 5 shows $\mu_n^{(v)}(\mathcal{X})$. Using Vecchia to fit the mean GP conditional on those variances (left panel of Figure 5) is harder because the R library does not allow the user to specify a vector of nuggets, which comprises \mathbf{S}_n in Eqs. (9–10). We inspected the source code to determine if modifications could accommodate \mathbf{S}_n but ultimately ended up implementing the following workaround instead.

We begin by fitting first moments with an otherwise ordinary Vecchia approximated GP, i.e., $\mathcal{GP}(D_n^{(m)})$, where $D_n^{(m)} = (\bar{\mathbf{X}}_n, \bar{\mathbf{Y}}_n)$. Let $\mu_n^{(m)}(\mathcal{X})$ denote the predictive mean of $\mathcal{GP}(D_n^{(m)})$. Note that $\mu_n^{(m)} \neq \mu_n^{\text{SK}}$ from Eq. (9) because the former utilizes a covariance structure with a single nugget, i.e., $\tau^2(k(\bar{\mathbf{X}}_n) + g\mathbb{I}_n)$ following Eq. (4), and the latter uses $\tau^2 k(\bar{\mathbf{X}}_n) + \mathbf{S}_n$. However, they are equal in expectation because GPs furnish unbiased predictors (see, e.g., Santner et al., 2018). Nevertheless the two can be quite different if the degree of replication is high because of the \mathbf{n} -vector in the denominator of Eq. (8). Specifically, if the replication degree varies significantly from one location to another, for instance $n_i \gg n_j$ for \bar{x}_i and \bar{x}_j , then the predictions from $\mu_n^{\text{SK}}(\mathbf{x})$ for \mathbf{x} in the vicinity of \bar{x}_j , the site with fewer replicates, could be considerably more precise than $\mu_n^{(m)}(\mathbf{x})$, which does not know to place less trust in \bar{y}_j than in other locations, such as near \bar{x}_i . However, in our setting we have uniform replication, with all $n_i = 31$. In a study described momentarily, and summarized in Figure 7, we find there is essentially no difference between $\mu_n^{(m)}$, via Vecchia, and μ_n^{SK} .

Approximating what SK provides for the variance of the first moment, $\Sigma_n^{\text{SK}}(\mathcal{X})$ in Eq. (10), with Vecchia, follows a similar thread. Whereas our development of the mean leverages the unbiased nature of Gaussian expectations, second moments follow standard calculations of

Gaussian variances. Crucially, we do not need the entire covariance structure $\Sigma_n^{\text{SK}}(\mathcal{X})$ for bias correction in Section 3.4; we only need the diagonal. Those “variances of the mean” are Gaussian standard errors, i.e., $\text{Var}\{Y(\mathbf{x})\}/n$, again leveraging uniform replication: $n_i = 31$. Our Vecchia fit to second moments provides an estimate of $\text{Var}\{Y(\mathbf{x})\}$ so all we need to do is divide this quantity by n_i , for any i , to get an estimate of the variance of the mean. However, we prefer a more conservative application of this in an SK-approximating context to avoid under-covering out-of-sample. Let $\mu_n^{(v)95}(\mathbf{x})$ denote the upper 95th quantile of predictive equations derived from $\mathcal{GP}(D_n^{(v)})$. We then combine this estimate with our first-moments’ fit, to obtain the following Vecchia approximation to SK.

$$(12) \quad \begin{aligned} \hat{\mu}_n^{\text{SK}}(\mathbf{x}) &= \mu_n^{(m)}(\mathbf{x}) \\ \hat{\sigma}_n^{\text{SK}}(\mathbf{x})^2 &= \mu_n^{(v)95}(\mathbf{x})/n_i + \sigma_n^{2(m)}(\mathbf{x}). \end{aligned}$$

Beyond missing off-diagonal covariance terms, this is an inefficient estimator compared to the ideal SK quantity in Eq. (10) because it does not borrow strength nearby in the input space. (This is what the term $-\tau^2 k(\mathbf{X}_n, \mathcal{X})^\top (\tau^2 k(\mathbf{X}_n) + \mathbf{S}_n)^{-1} \tau^2 k(\mathbf{X}_n, \mathcal{X})$ in that expression is doing.) So in $\sigma_n^{2(m)}(\mathbf{x})$ we’re getting over-inflated, conservative UQ.

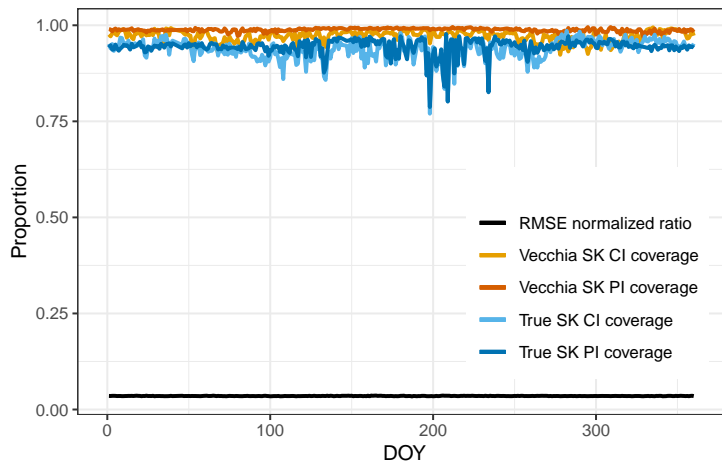


FIG 7. Out-of-sample scaled RMSE ratio and 95% confidence and prediction interval (CI and PI, respectively), corresponding to true SK and our SK approximation over day of year (DOY) in 2022. The root mean-squared error (RMSE, smaller is better) ratio is calculated relative to the RMSE values of true SK, scaled by the range of temperature values present in the data (28.54°C).

To benchmark our Vecchia-based workaround for SK we developed the following exercise to compare our SK approximation to true SK with respect to out of sample prediction accuracy and UQ. We used a subset of our corpus of NOAA-GLM runs. The goal was to have a large enough training exercise to stress our Vecchia calculations, while not being too large as to preclude expedient ordinary-GP calculations behind SK. We divided up one year’s worth of NOAA-GLM hindcasts, including all depths and horizons, into five-day chunks. For each chunk we used a random $n_i = 16$ sample of NOAA-replicates for training, setting aside the other 15 for out-of-sample testing. In this way, each training data set was manageably sized at $n = 1600$ unique inputs. For each of the seventy-three spans of five days in 2022 we fit SK (9–10) and the Vecchia-approximated first- and second-moments, $\mu_n^{(m)}$ and $\sigma_n^{2(m)}$ for the mean and $\mu_n^{(v)}$ for full predictive uncertainty in Eq. (12), respectively. We saved out-of-sample RMSEs and coverages of 95% CIs and PIs. The calculation of CI coverage involved

averages of the fifteen held-out replicates, at each unique input, whereas PIs used all of the hold-out replicates individually.

Figure 7 provides a compact summary of the results of that experiment. PI/CI coverages are shown as a proportion. PIs (dark blue) for both the approximate and true SK are fairly consistent throughout the year, whereas CIs (light blue) fluctuate slightly more over DOY. Average CI coverages over the entire year for the approximation and true SK are 97.2 and 93.8%, respectively, while average PI coverage for true SK and the approximation are 94.5 and 99%. We attribute the slightly higher variability in CI coverage of both methods to the relatively small 5-day training data size that was entertained. With only five days of examples to train on, there is not much diversity along the time axis in order to stabilize variances of first moments. Overall, coverage of our Vecchia-based SK approximation (12), via $\hat{\mu}_n^{\text{SK}}(\mathbf{x})$ and $\hat{\sigma}^{\text{SK}}(\mathbf{x})^2$ is slightly higher than that of SK, which is by design (12). The black line at the bottom of the figure compares root mean-squared errors (RMSEs) obtained from true SK to our Vecchia approximation via a ratio scaled by the range in temperatures at all depths and for all days in 2022 (28.54°C). A value near 0.035, with little fluctuation, indicates that true SK and Vecchia are in agreement with respect to predictive accuracy,

We are encouraged by these results. True SK is not tractable on larger problems. Our Vecchia approximation can be fit on millions of NOAA-GLM runs in mere seconds, and we are confident that it closely matches the performance of SK.

3.4. *Modeling forecast bias.* Let $\hat{\mu}_n^{\text{SK}}(\mathbf{x})$ and $\hat{\sigma}^{\text{SK}}(\mathbf{x})^2$ denote the moments of our NOAA-GLM surrogate (12), as described in Section 3.3 but fit to the entire campaign of runs across all 31 ensemble members and all training days/horizons/depths under study: $(\mathbf{X}_{n_M}, \mathbf{Y}_{n_M})$. A fit based on these 8 million-odd runs, spanning three years of simulations, could only be fit via an approximation such as with Vecchia. Providing $\mathbf{x} \in \mathcal{X}$ representing any time point(s) of interest (future, present or past), including depths and horizons of interest, yields a prediction (or forecast) capturing uncertainty in GLM dynamics driven by NOAA ensemble hindcasts. Recall from Section 2.2 that estimating a bias correction requires measuring discrepancy between computer model predictions and field data observations, forming a data set D^b that can be used to train a GP. Our field data are a single set of observations $\mathbf{Y}_{n_F}^F$ in time and depth, coded in \mathbf{X}_{n_F} . In Section 2.2 we had $\mathbf{X}_{n_F} = \mathbf{X}_{n_M}$, so $\mathbf{Y}_{n_F}^F$ could easily be lined up with predictions μ_{n_M} to measure discrepancies (6). However, now our set of GLM inputs (and outputs) is expanded [Section 3.1] to encompass horizon, which is not relevant to our field sensor measurements. Field data and surrogate are out of alignment.

We must construct an field data response vector $\bar{\mathbf{Y}}_{n_F}^F$ whose length and composition matches that of $\bar{\mathbf{X}}_n$, comprising unique inputs to our computer model up to the ensemble member, e , which are treated as replicates in our Vecchia approximation to SK. This requires inserting multiple copies $\mathbf{Y}_{n_F}^F$ into $\bar{\mathbf{Y}}_n^F$ in such a way that they line up with the simulation parameters corresponding to the time/depth/horizon parameters in $\bar{\mathbf{X}}_n$. For example, suppose \mathbf{x}_i^\top , residing in the i^{th} row of $\bar{\mathbf{X}}_{n_F}^F$ records a particular time t_i and depth d_i measurement of lake temperature. Then, we must place y_i , the i^{th} entry of the vector $\mathbf{Y}_{n_F}^F$, in all 30 slots $\bar{\mathbf{Y}}_{n_F}^F$ that match up with the \mathbf{x} -tuple $(t_i - h_i, d_i, h_i)$ in $\bar{\mathbf{X}}_n$.

We may now define a data set of discrepancies, following Eq. (6), $D_n^b = (\bar{\mathbf{X}}_n, \bar{\mathbf{Y}}_{n_F}^F - \hat{\mu}_n^{\text{SK}}(\mathbf{X}_n))$, and fit $\mathcal{GP}(D_n^b)$ to characterize a bias correction over time/depth/horizon. The size of n again makes full GP fitting prohibitive, so we use a Vecchia approximation. However, we do not have the luxury of replication, so we must opt for an ordinary, homoskedastic GP fit. Let $\mu_n^b(\cdot)$ and $\sigma_n^{2b}(\cdot)$ denote the moments of this GP fit, overloading our earlier Section 2.2 notation. A GP surrogate with bias-correction (GPBC) may be formed by chaining the two sets of predictive moments together.

$$(13) \quad \mu_n(\mathcal{X}) \equiv \hat{\mu}_n^{\text{SK}}(\mathcal{X}) + \mu_n^b(\mathcal{X})$$

$$\sigma_n^2(\mathcal{X}) \equiv \hat{\sigma}_n^{\text{SK}}(\mathcal{X})^2 + \sigma_n^{2b}(\mathcal{X})$$

As in Section 2.2, $\sigma_n^2(\mathcal{X})$ over-estimates the variance of the sum of two GP variances because it is missing a negative covariance term. In contrast to the discussion in Section 2.2, we cannot utilize full predictive covariance matrices $\Sigma(\mathcal{X})$ because the Vecchia implementation we use only provides the diagonal, which is what we are denoting as $\sigma^2(\mathcal{X})$. We may put in for \mathcal{X} anything we wish; however, the most useful settings indicate hindcasts (\mathcal{X} depicting a historical set of forecasting days, horizons, and depths) and forecasts (\mathcal{X} denoting the current day, a horizon of the next thirty days, and all depths of interest).

To illustrate, Figure 8 shows examples of 1m-depth “slices” of hindcasts via quantities defined above starting on Feb. 19, 2021 (left), 2022 (middle) and 2023 (right). Consider the top row (denoted as A) first. Each gray line is a NOAA-GLM hindcast over a 30-day horizon. Orange lines summarize the computer model surrogate ($\hat{\mu}_n^{\text{SK}}$ and $\hat{\sigma}_n^{\text{SK}}$ via 90% error bars), denoted as GPGLM.⁴ Purple dots show the $\bar{Y}_{n,F}^F$ corresponding to that date/depth and each horizon. Discrepancy data D^b , derived from the $\hat{\mu}_n^{\text{SK}}$ and $\bar{Y}_{n,F}^F$, are shown at the bottom of each panel. Observe that in all three panels/years, these fits exhibit a cold bias because the bias correction is positive. The strength and statistical significance of this conclusion varies considerably across the three years. In 2021 correction from zero might not be statistically significant. But in 2022 and 2023 it is substantial (upwards of 3 degrees), highly non-linear, and error-bars do not cover zero over most of the 30-day horizon.

The bottom row of the figure (denoted as B) shows how Eq. (13) is used to combine the quantities in the top row in order to provide the bias-corrected surrogate (GPBC). Observe that in all three years this provides a very good approximation to sensor measurements. PI coverage is excellent. Note that while PIs for the surrogate in the top/A panels exhibit a trumpet-like shape over increasing horizon, those in the bottom/B panels no longer have this pronounced shape. This is because our bias correction is homoskedastic.

Figure 9 shows a similar pair of views, but now in a forecasting context corresponding to the right-most column of Figure 8 (2023). Specifically, we mean that the gray lines, from the GLM were used to build the surrogate (along with simulations for all other days/depths in the past), but the field data (purple dots) are not observed. Thus, bias correction is based only on patterns learned on *historical* data. We chose this particular case to illustrate because it represents a challenging one. Although the overall predictive quality in Figure 9 is lower than the right column of Figure 8, because the former is in-sample and the later is out-of-sample, it is clear the the GPBC performs well. Visually, the bias correction is effective (panel B) compared to the surrogate on it’s own (panel A). This can also be quantified as follows, offered here as a precursor to a more exhaustive validation described next in Section 5: GPBC achieves an RMSE of 1.24°C compared to 1.86°C GPGLM on it’s own. Note that while PI coverage is lower for GPBC for this particular example, the width of the PIs of GPBC (2.23) is less than half of the PI width of the surrogate on its own (5.14).

4. Real-time forecasting. We now have all of the ingredients in place to build a real-time forecasting system combining simulated and observed temperatures. By “real-time,” we mean that forecasts can be updated daily, in a matter of minutes, when new field data (sensor measurements) and data products (NOAA forecasts) arrive. We have ensured that the process of fitting surrogates and bias correction is swift, so the primary delay comes from awaiting updated data. Here we elaborate on the configuration of our real-time system, with

⁴We use the full PI here, via $\mu^{(v)}$, instead of $\sigma^{2(m)}$ providing a CI, which is used in the GPBC, as the former is easier to see. These are also what you would use if you were predicting via the surrogate alone, without bias correction. An example of the latter is shown in Figure 6.

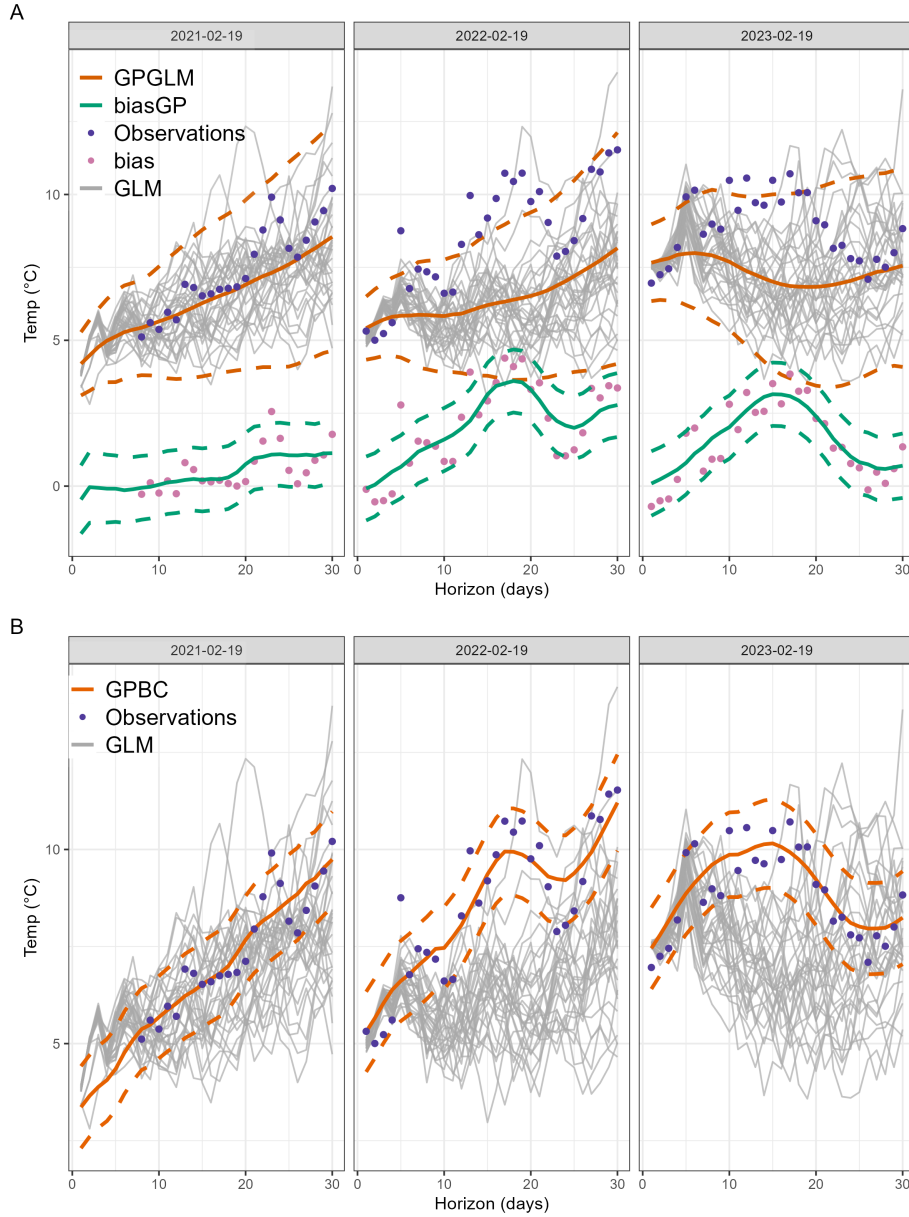


FIG 8. NOAA GLM forecasts (gray lines) starting on Feb. 19 for years 2021, 2022, and 2023 at a depth of 1m. Sensor measurements (purple points) are overlaid. Row A: In-sample predictions and 90% PIs from the GLM surrogate (GLMGP, orange). Means and PIs for the bias GP (biasGP) in teal; raw bias in magenta. Row B: In-sample forecasts (predictive means) and 90% PIs for the bias-corrected GLM surrogate (GPBC, orange). Means and PIs for the bias GP in teal; and bias in magenta.

an emphasis on the principal variation based on Vecchia/SK, as described in Section 3, while also accommodating more straightforward alternatives earlier. We then describe a variation that we developed in order to allow forecasts to react more dynamically to the most recent observational and simulation data, and to data from the most similar previous years.

4.1. *Iterative forecasting.* Our forecasting framework consists of: an initial training stage, in which many historical NOAA-GLM simulations are used to fit a GP surrogate $\mathcal{GP}(D_{n_M}^b)$ and bias correction $\mathcal{GP}(D_n^b)$; and an iterative stage, in which new data is down-

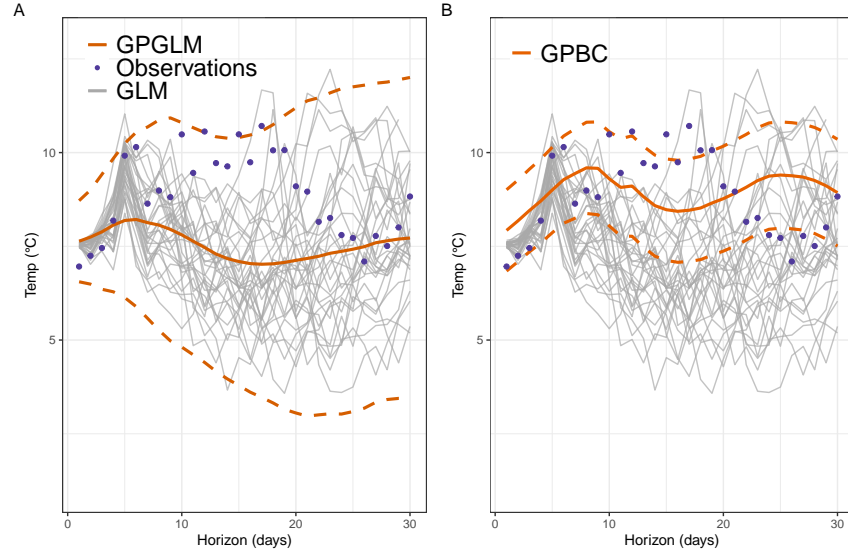


FIG 9. NOAA GLM forecasts (gray lines) starting on Feb. 19 for year 2023 at a depth of 1m; sensor measurements are shown in purple. Panel A shows the in-sample prediction from the GLM surrogate as depicted in 8 (right panel). Panel B shows the out-of-sample forecast from the bias-corrected GLM surrogate.

loaded, existing datasets are updated, and a new forecast is generated from the (updated) surrogates. Here we are using \mathcal{GP} generically, since many variations are possible. The initial training phase begins with obtaining NOAA-GLM simulations (hindcasts) for all reference dates in the historical training period. A surrogate fit to these data provides a statistical abstraction of NOAA-GLM simulations over the historical period of time. Observed residuals relating sensor data to surrogate predictions may be used to estimate a bias correction.

The iterative phase (Fig. 10), which happens daily, is more interesting. This begins with downloading NOAA ensemble forecasts over the next thirty days. Next, these weather forecasts are fed as driver data to the GLM, augmenting the simulation campaign from the training phase, and updating the surrogate and bias correction accordingly. The bias-corrected surrogate can then be used to make lake temperature forecasts over that thirty-day period. The process wraps up, before repeating the next day, by observing actual temperatures on the current day from sensors at each depth. Our implementation is faithful to that description, but is more accurately described by an operation that is performed all at once in a matter of minutes at midnight (00UTC), separating “yesterday” from “tomorrow”. This is when NOAA forecasts for “tomorrow” (and the 29 subsequent days), and sensor measurements from “yesterday” become available. Yesterday’s sensor measurements can be used to validate previous forecasts, and the metrics we prefer are discussed next in Section 5.1. NOAA forecasts can be fed into GLM to produce 1–30 day-ahead lake temperature forecasts over each horizon and depth of interest. Those NOAA-GLM forecasts are then incorporated into the corpus of existing simulation training data, along with the sensor measurements. Model fitting for surrogates and bias correction can then again be carried out, for example as described in Sections 3.3–3.4. Although there is potential for computational economy in priming aspects of new fits from previous ones, we do not generally bother because the Vecchia-based methods are fast. Updated surrogates may then be used to generate a 1–30 day-ahead bias-corrected forecast. The process repeats again at the next midnight as part of the iterative, near-term forecasting cycle (Dietze et al., 2018).

4.2. *Incorporating annual variability into forecasts.* The inputs to our surrogate modeling and bias correction framework are Julian day $t \in \{1, \dots, 365\}$, depth $d \in \{0, \dots, 9\}$, and

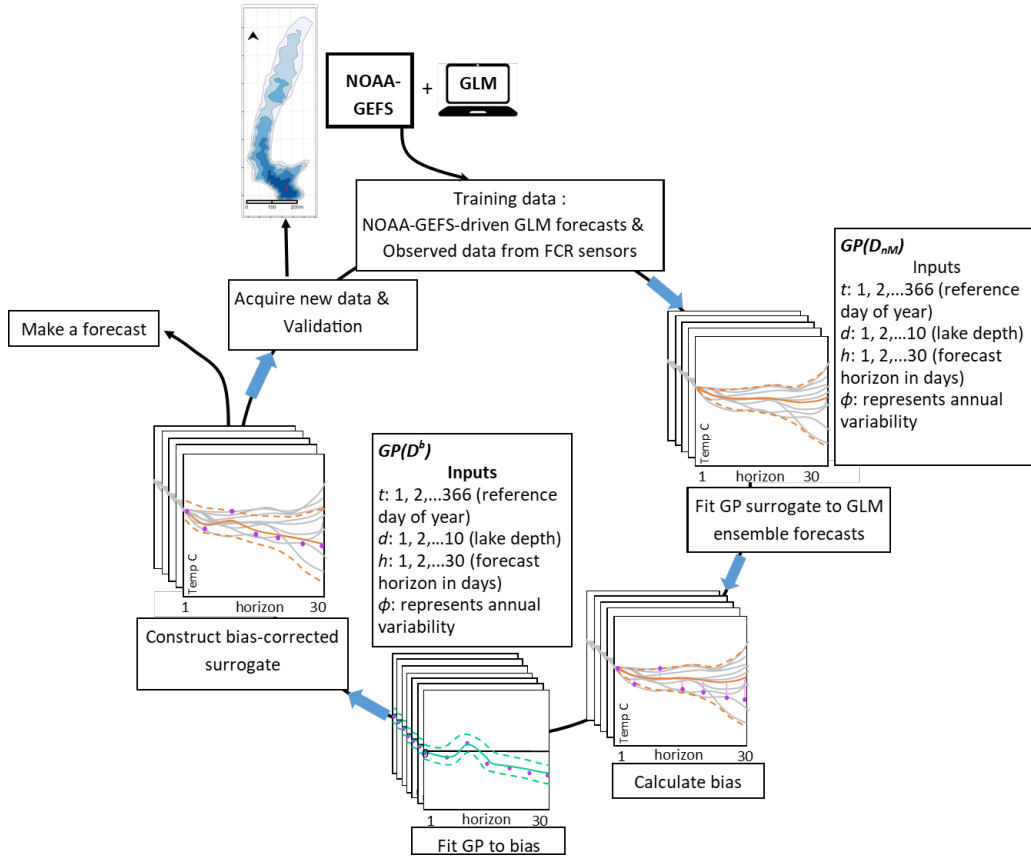


FIG 10. Iterative workflow for generating daily, 1–30 day-ahead forecasts of lake temperatures at 10 depths.

horizon $h \in \{1, \dots, 30\}$. A consequence of this choice, especially with regard to the time input t , is that our forecasts will be identical for any day t in any year. We have a “day of year” model, meaning that a forecast for today would be the same as a hindcast starting on that same day in any year represented in the training data or beyond. (Those hindcasts would differ, of course, from what we would have forecast at earlier times, as the training data of NOAA-GLM simulations and observations is augmented every time a forecast is made). As we gather more data, such “day of year” forecasts will have more conservative UQ because they will have been trained on a wider diversity of observations across year for that day, and days nearby in time. In other words, they will better capture climatological variability. But they will, as more time passes and data is gathered, be less reactive to current weather patterns and other environmental variables.

To illustrate, consider the left column of Figure 11, which shows examples of predictions over a 30-day horizon for March 3 2023 at depth 1m from the surrogate only (top panel) and after bias correction (bottom). As with similar figures shown previously, forecasts are in orange (solid mean and dashed intervals), with sensor measurements as purple dots. In contrast to previous visuals, we now show all three sets of NOAA-GLM simulations available up until this time point: today’s (March 3 2023) in black and the previous two years (March 3 in 2022 and 2021) in gray. Observe that the orange forecasts do a poor job of tracking with today’s black simulations. In the top row, forecasts from the surrogate track the corpus of simulations, whereas in the bottom row their spread is narrowed somewhat by the bias correction, but in an overly conservative fashion.

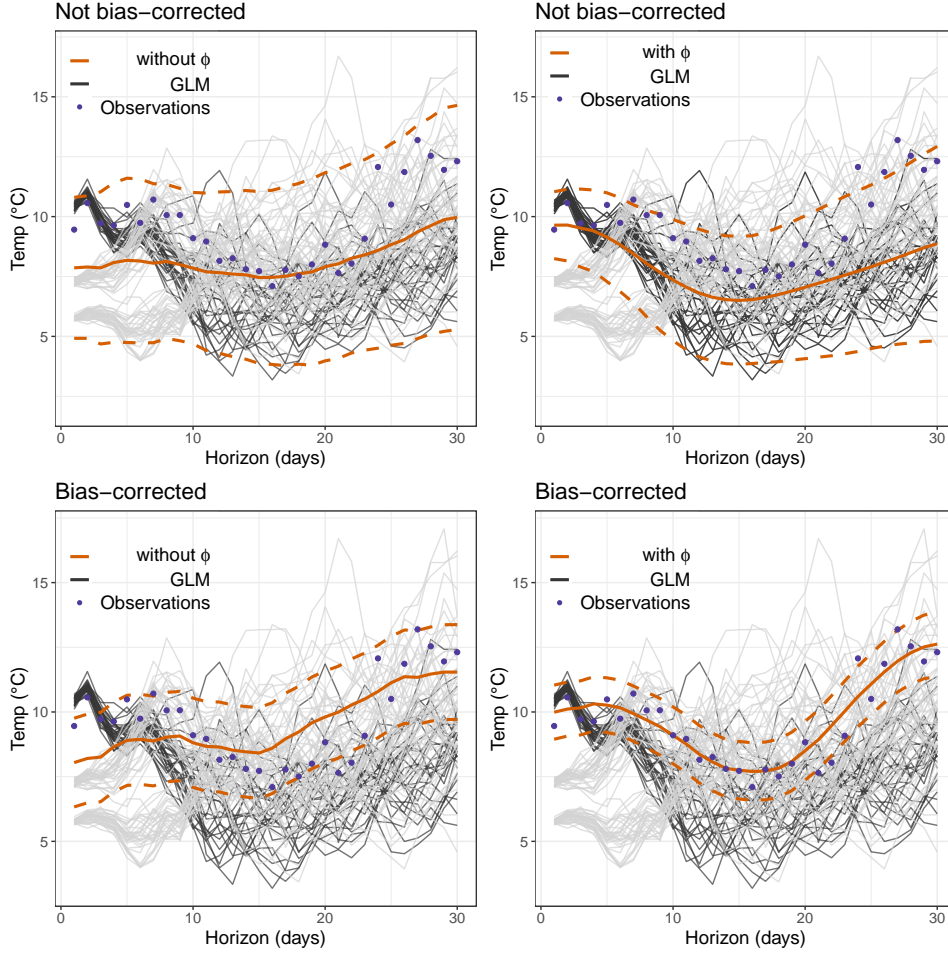


FIG 11. *In-sample forecasts for March 1, 2023 from forecasting models without ϕ (“without ϕ ”) and those with ϕ (“with ϕ ”) at 1m depth; 90% prediction intervals are denoted by dashed lines. Sensor measurements are shown in purple. GLM forecasts for March 1, 2023 are shown in dark gray; previous years are shown in light gray.*

Toward obtaining more dynamic forecasts, we introduce a fourth input variable, which we call ϕ , whose behavior is illustrated in the right panels in the figure and is described as follows. With ϕ we aim to capture the unique “state” for day t and year λ [first introduced in Section 3.1], via the following calculation

$$(14) \quad \phi(t, \lambda) = \frac{1}{5} \sum_{i=0}^4 \left(\frac{\mathbf{Y}_{n_F}^F(t-i, d=0, \lambda) + \mathbf{Y}_{n_F}^F(t-i, d=1, \lambda)}{2} \right),$$

capturing the average sensor-measured temperatures near the surface (depths zero and one meters) over the previous five days. We then augment design matrices $\bar{\mathbf{X}}_n$ and $\bar{\mathbf{X}}_{n_F}^F$ to include $\phi(t, \lambda)$ matching up with t and λ already recorded in its rows. (Recall that the λ column is ignored in our GP modeling, but now with the addition of ϕ its presence is felt through the state that it captures (14)). Surrogate modeling and bias correction, as described in Sections 3.2–3.4, are not affected by this change excepting the higher input dimension, and corresponding additional lengthscale(s). In particular, responses $\bar{\mathbf{Y}}_n^M$ and $\mathbf{Y}_{n_F}^F$ remain as before.

To see the effect of adding ϕ as a predictor consider the right column of Figure 11. Observe how, in contrast with the left column without ϕ , the GLM surrogate without a bias-correction (top/orange) provides a good fit to NOAA-GLM forecasts (black lines). When bias-correction

is added (bottom/orange), prediction intervals narrow considerably and appropriately compared to the sensor measurements (purple dots). We generally find better results with the addition of ϕ , as we shall demonstrate momentarily in Section 5. Consequently, we shall going forward take the ϕ version to be the main/default modeling variation unless we mention that modeling “without ϕ ” was entertained as a contrast. In fact, all previous visuals in the paper used the version with ϕ , because they looked better. The diagram in Figure 10 lists ϕ as one of the inputs. Of course, Eq. (14) is only one of possibly many ways that a year-differentiating state could be calculated. It could even be treated as a latent variable, to be inferred along with other unknowns, which we discuss as a possible extension in Section 6.

5. Out of sample results. Here we lay out evaluation metrics and comparators and then describe an out-of-sample exercise designed to explore the relative merits of GPBC forecasts, concluding with an analysis of results.

5.1. Validation and benchmarking. When new sensor measurements come in at mid-night, for “yesterday”, we have the opportunity to assess the accuracy of our forecasts for that day, as predicted on all thirty previous days at varying future horizons. In our assessments, we record (1) RMSE as a measure of accuracy; (2) a proper log score (Eq. (25) of [Gneiting and Raftery, 2007](#)) combining accuracy and UQ out of sample; and (3) confidence interval width and (4) coverage. Given predictions $\hat{\mu} \equiv \hat{\mu}(\mathcal{X}) = (\hat{\mu}_1, \dots, \hat{\mu}_N)^\top$ for out of sample $Y \equiv Y(\mathcal{X}) = (y_1, \dots, y_N)^\top$ score and RMSE may be calculated as follows:

$$\text{RMSE}(Y, \hat{\mu}) = \sqrt{\frac{1}{N} \sum_{i=1}^N (y_i - \hat{\mu}_i)^2}$$

$$\text{score}(Y, \hat{\mu}, \Sigma) = -\log |\Sigma| - (Y - \hat{\mu})^\top \Sigma^{-1} (Y - \hat{\mu}).$$

Smaller RMSEs and larger scores are preferred. When validating for multiple horizons, and/or over multiple days, we aggregate accordingly. Score, RMSE, interval width and coverage are interesting because they provide a general sense of how the forecaster is performing. However, they are most useful when benchmarking against other, competing frameworks.

As comparators we consider the following four methods. Each is simplification of flagship GPBC (with ϕ) approach, missing one or more of its building blocks.

GPGLM: a GP surrogate for GLM without bias-correction (GPGLM), but otherwise using all predictors (including ϕ) as well as Vecchia/SK features for heteroskedastic modeling and fast computation. The setup here follows Figure 10 for iterative updating, but skipping the bottom left bias-correction corner of the circuit.

GPO: a heteroscedastic GP fitted to observed sensor measurements only, using Julian day of year and depth as inputs (no ϕ). For this competitor, we do not follow Figure 10. The resulting forecasts simply reflect a “typical” year based all previous years’ measurements. Importantly, GLM’s short-term forecasts are not used at all. In this way, GPO represents a “climatological” model, as its predictions reflect typical seasonality and general trends. Here, since the sensor data set is relatively small ($365 \times 10/\text{year}$) we do not need the Vecchia approximation, so we opted for a heteroskedastic GP fit from the `hetGP` R package ([Binois and Gramacy, 2021](#)) via `mleHetGP`. A `hetGP` fit is similar to SK [Section 3.2], but with joint inference for first and second-moment GPs, which is crucial when the degree of replication is low. Recall that SK requires a moderate degree of replication, and there is no replication in the sensor measurements.

GLM: raw 1–30 day-ahead NOAA-GLM forecasts in the testing time period. For this competitor, we calculated empirical means and standard deviations over all 31 ensemble members for all combinations reference date, depth, and horizon in the test time period.

GPBC without ϕ : a bias-corrected surrogate for GLM where the input ϕ (providing annual variability) is omitted. Like GPO, this competitor is climatological, as its forecasts are based only on historical information. However, it does incorporate NOAA-GLM hindcasts and as forecasts for the current day, so it is not a purely historical model.

Each benchmarking comparator offers a glimpse into the potential benefit, or hazard, of higher fidelity modeling via the components that make up GPBC. GPGLM illuminates the value of bias correction, whereas GLM (which does not include a bias-correction) illustrates the value of surrogate modeling, as opposed to using raw simulations. Climatological models, like GPO and GPBC without ϕ , are often hard to beat on longer time scales (Thomas et al., 2020), i.e., in situations where dynamics are more climate- than weather-driven. Weather forecasts become rapidly more inaccurate more than a week into the future. Although we would hope that our principal model, GPBC, would be capable of detecting and correcting for those inaccuracies, there is always estimation risk inherent in additional complexity. In other words, it could be better to simply ignore weather predictions for longer horizons.

5.2. Forecasting exercise. Our exercise simulates one year of daily forecasting (e.g. Figure 10), beginning June 11 2022, and ending on the same day in 2023, treating a corpus of model runs and sensor measurements from October 3 2020 through June 10 2022 as training data which is augmented daily. GPBC and GPGLM model fitting is as described in Section 3. Training data for GPO consisted only of sensor measurements comprising the initial training period before June 10 2022. We present our results in several views.

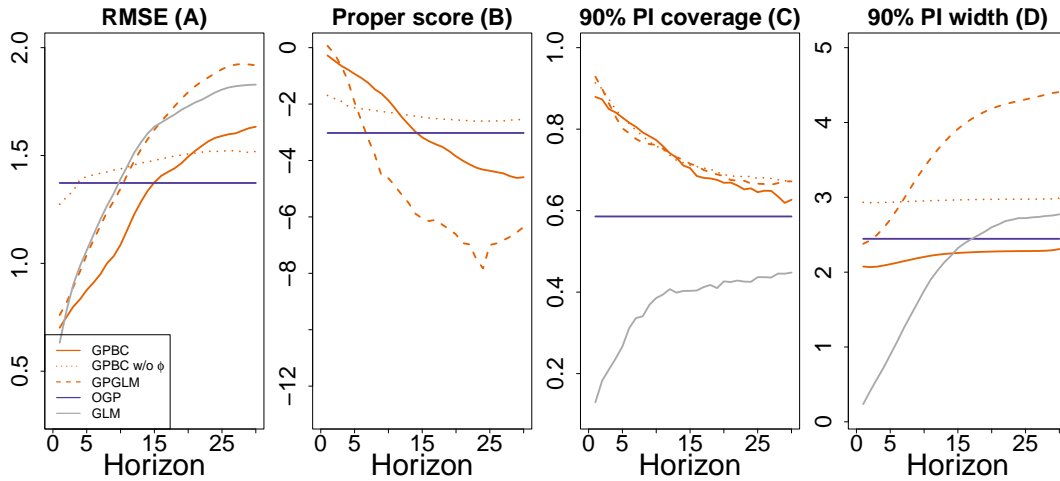


FIG 12. *RMSE* ($^{\circ}\text{C}$), *proper* (log) *score*, and *90% PI coverage*, and *PI interval width* from left to right respectively, summarizing from out-of-sample forecasts for all competing models over horizon. Scores of GLM were omitted from the panel B because they were many orders of magnitude lower than other competitors.

Figure 12 shows RMSE, score, coverage, and PI width for each horizon, aggregating over all depths and days in the forecasting period. First consider RMSE in panel (A), where lower is better. Observe that every method outperforms OGP, the purely sensor-based climatological benchmark, at short horizons. This is a testament to the value of NOAA-GLM in the short term. However, OGP outperforms every other method after about two weeks out. We suspect this is because NOAA forecasts are unreliable at long horizons. In the shorter term, those methods that are most influenced by GLM forecasts perform best. Standalone GLM forecasts or GPGLM (with the surrogate) have similar performance. Improvements in accuracy due

to the bias-correction in GPBC (with ϕ) is clearly evident, being consistently better than both GPGLM and GLM. However, at more than two weeks out, climatological forecasts (OGP) are most accurate. Omitting ϕ compromises the influence of GLM forecasts, which results in some advantages as well as disadvantages. Over short horizons, this comparator underwhelms, but at longer horizons its forecasts are more robust, similar to OGP.

Next consider the panel (B) of the figure, which summarizes scores over horizon (higher is better). Overall trends here are similar to the RMSE panel, with some notable exceptions. The raw GLM's score falls outside the lower range of the y -axis, so a line for this comparator does not appear on the plot. Although it was reasonably accurate in terms of RMSE (left panel), it has poor UQ, which we shall discuss next with panels (D–E). Again, our flagship GPBC comparator performs best for the first two weeks, except horizon one, where the surrogate-assisted GLM (GPGLM) has a better score than GPBC. However, like raw GLM, this comparator is exceedingly poor at higher horizons. Observe that GPBC without ϕ is the best comparator for horizons longer than two weeks. In particular, it beats the purely sensor-based climatological comparator.

Panel (C) summarizes empirical coverage from 90% predictive intervals over horizon. Only the methods using surrogate-assisted NOAA-GLM forecasts can achieve nominal coverage (at 90%) at any horizon. Raw-GLM dramatically under-covers. Its surrogate (GPGLM), by contrast, is able to correctly quantify uncertainty by accessing the entire corpus of simulations across the years. Although empirical coverage drops off from nominal at higher horizons, models that incorporate GLM forecasts (GPBC and GPGLM) always outperform OGP, the climatological benchmark. Additional insight into these coverage results is provided by panel (D). Observe that the PIs of raw GLM forecasts are much narrower than those from other competitors, especially at early horizons. We also know (e.g., Figure 8) that standalone GLM simulations and forecasts can exhibit pronounced bias. Taken together, this explains raw GLM's poor scores (panel B). Also note that PIs resulting from GPGLM are twice as wide as those of GLM for all horizons. Although GPBC and GPGLM have similar PI coverage, PIs of GPBC are much narrower than those of GPGLM. In fact, at horizon 30, PI width of GPBC (2.2) is nearly half that of GPGLM (4.2). Together, results show that bias-correction not only increases accuracy (via RMSE in panel A) but also results in narrower PIs. Note that although GPBC utilizes a homoskedastic GLM surrogate, PI interval width expands only slightly over horizon because the bias correction is homoskedastic.

Figure 13 shows RMSE (A), score (B), coverage (C), and PI width for each depth (D), where results are aggregated over all horizons and days in the forecasting period. Similar to RMSE results over horizon, all competitors relying on GLM forecasts outperform OGP at deeper (>3m) depths, while OGP performs best at shallow depths (1–3m). NOAA-GLM forecasts can be highly variable at shallow depths, which may explain why forecasts from all GLM-surrogate assisted methods are less accurate than those of OGP at shallow depths. In contrast to RMSE results aggregated over horizon, GPBC (without ϕ) is consistently less accurate than GPBC (with ϕ). When examining RMSE results over depth, the improvement in accuracy provided by bias-correction in GPBC is not quite as dramatic as RMSE results summarized over horizon, but bias correction is still helpful.

The story is similar for proper scores. GPBC attains better (larger) scores than all other competitors at deeper depths. At shallow depths, GPBC (without ϕ) performs slightly better than its “with ϕ ” counterpart. However at deeper depths, both variations of GPBC perform similarly. At surface and 1m depths, OGP and GPGLM perform best, but after 1m, GPGLM's scores fall steadily until 4m depth. As with results over horizon, raw GLM's scores fall beyond the y -limit range of the plot. Though raw GLM's accuracy over depth is similar to that of GPGLM, its UQ (discussed next) is poor, resulting in very low scores.

Coverage for all competitors except GPBC generally declines over depth, with some exceptions. While coverage of all other competitors decreases quickly after 1m depth, empirical

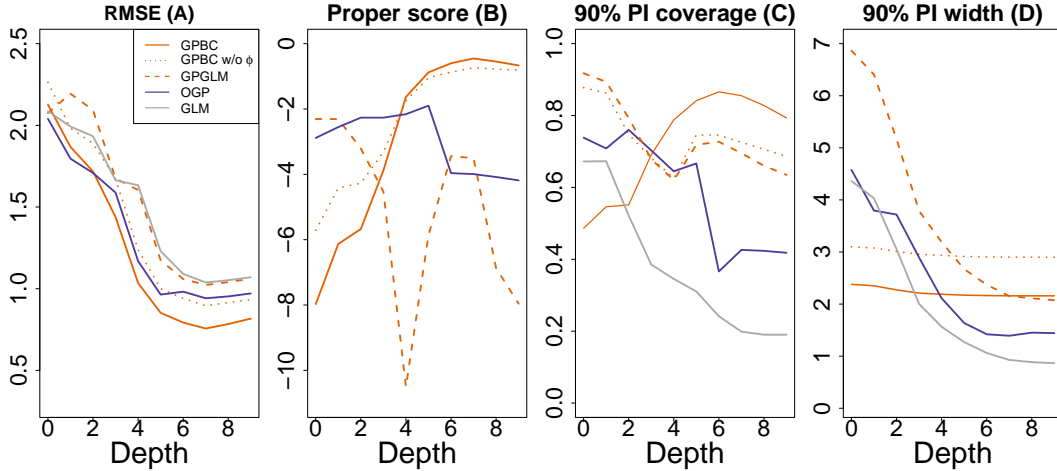


FIG 13. *RMSE* ($^{\circ}\text{C}$), *proper (log) score*, and *90% PI coverage*, and *PI interval width* from left to right respectively, summarizing from out-of-sample forecasts for all competing models over depth. Scores of GLM were omitted from the panel B because they were many orders of magnitude lower than other competitors.

coverage of GPBC actually increases steadily to 90% at 6m depth, declining to 80% at 9m depth. Even at 9m depth, GPBC still attains 80% coverage while other methods achieve only between 20 and 65% empirical coverage. GLM performs poorly overall, achieving a maximum empirical coverage of 68% only at surface depth. Finally, PI widths over depth for all competitors gradually decrease with increasing depth. A similar pattern exhibited in results over horizon is again apparent: PI widths of GPGLM are nearly three times as wide as those of GPBC at shallow depths. In addition, PI widths of GLM, and to some extent OGP, are much narrower than those of all other competitors at depths $>3\text{m}$. GLM’s poor scores can be attributed to poor PI coverage over depth and inherent bias, and similarly, OGP’s declining PI coverage over depth can likely be attributed to a decrease in PI width over depth.

Figure 14 offers another perspective by focusing on forecasts over day of year (DOY) for two forecast horizons (1 and 30 days into the future). The top panel shows one-day ahead forecasts generated by GPGLM and GPBC, while the bottom panel shows forecasts at 30 days into the future at five depths. Observe in the top panels (one-day ahead) that GPGLM and GLM are generally in agreement with observations. In fact, for the majority of days of the year and all depths, forecasts and observations lie nearly on top of one another. At thirty days out (bottom panels), the discrepancies between forecasts from GPGLM and GPBC are much more apparent, especially for deeper depths. At surface depths, the effect of bias-correction is not as obvious, but the improvement from bias-correction clearly results in enhanced forecast accuracy at deeper depths between DOY 1 and 240. Taken together with main results over depth and horizon in Figures 12–13, the visual here reinforces the importance of a bias-correction in improving accuracy over depth and horizon.

Next, Figure 15 shows how raw GLM bias (gray) surrogate GLM bias (“actual bias” via $\bar{Y}_n^F - \hat{\mu}_n^{\text{SK}}(\bar{X}_n)$), and predicted bias vary over DOY in our out-of-sample forecasting exercise. Observe that while accuracy varies over horizon [Figure 12] the magnitude of bias from GLM depends even more strongly on the time of year a forecast is made [Figure 15]. Bias from GLM and its surrogate are similar. Predicted bias, which is used to correct it, follows a similar pattern, but it is not perfectly aligned with actual bias: it underestimates for the first half of the year, and then overestimates in the second half. Note that the predicted bias is not smooth, because bias for each day in the forecasting period was predicted iteratively (following Figure 10), so each prediction was based upon a slightly different GP fit.

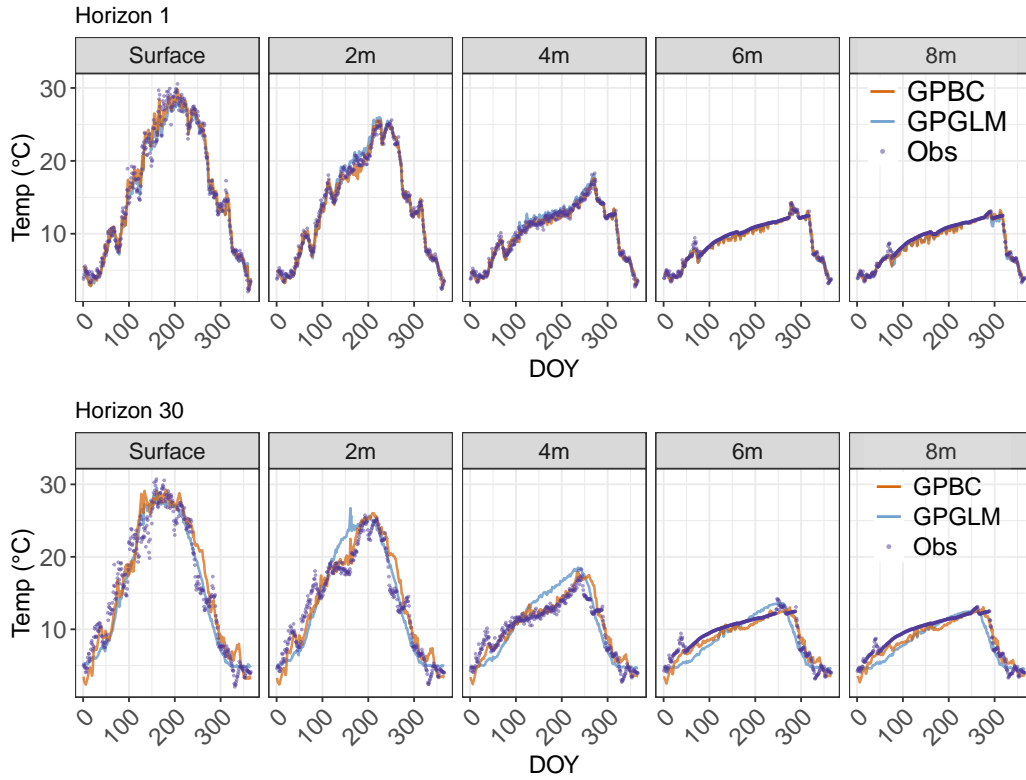


FIG 14. Forecasts from GPGLM (blue) and GPBC (orange) generated during the forecasting exercise for horizon 1 (one day into the future, top) and horizon 30 (30 days into the future) over day of year (DOY) at surface, 2, 4, 6, and 8m depths (each panel denotes one depth). Observations are shown in purple.

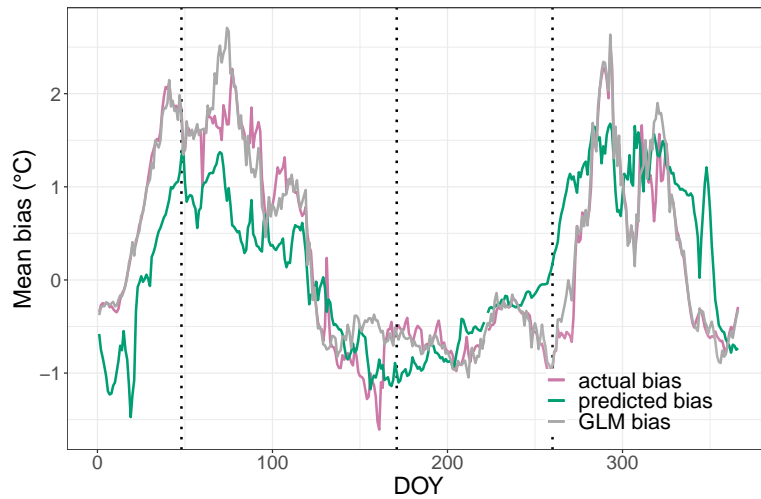


FIG 15. Bias (e.g., $\bar{Y}_n^F - \hat{\mu}_n^{SK}(\bar{X}_n)$) for out-of sample forecasts from the GLM surrogate (pink), raw GLM (gray) and predicted bias (teal), averaged over depth and horizon for dates in the testing time period. Vertical black dashed lines denote example DOYs depicted in Figure 16.

Finally, Figure 16 augments the visual in Figure 15 by breaking out horizon and depth contributions to the bias for three particular days (indicated as vertical dashed lines in Figure

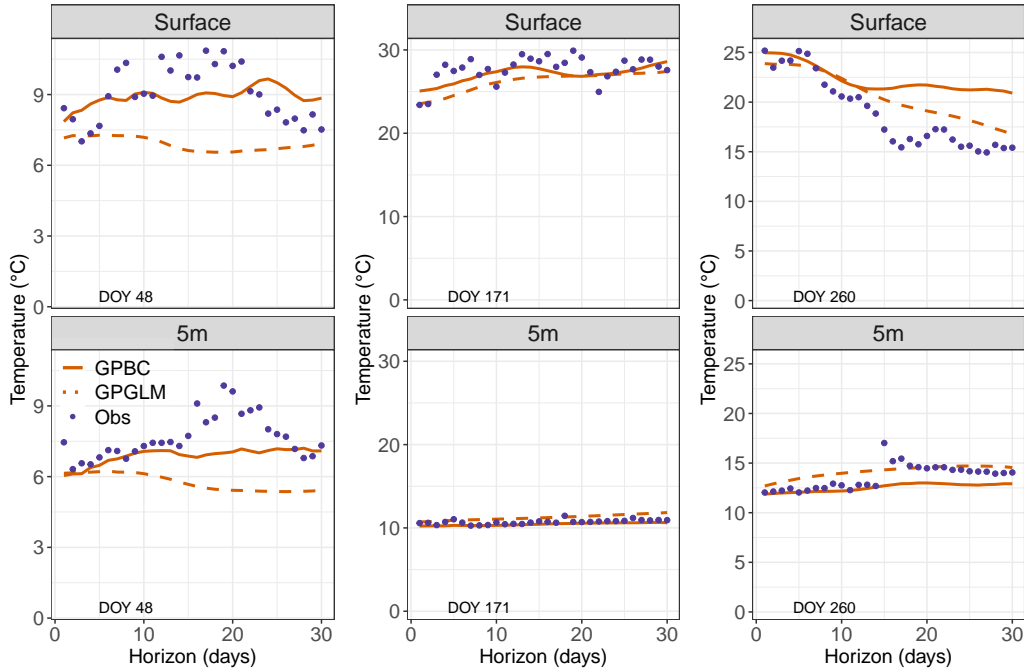


FIG 16. Out-of-sample predictive means of GPBC and GPGLM in orange solid and dashed lines, respectively, as well as observations in purple for 0m and 5m depth for the three days highlighted in Figure 15: 48, 171 and 260.

15). These three example days were chosen to display occasions when the bias-correction was correct in sign but not in magnitude (DOY 48 and 260) and generally correct in sign and magnitude (171). Consider DOY 48 first, in the left panels of Figure 16. Applying a bias correction (GPBC) improves the accuracy of forecasts compared to the GLM surrogate without a bias correction (GPGLM) with respect to observations (purple dots) at both 0 and 5m depths, although at 5m depth the forecast is still characterized by a cold bias. Moving to DOY 260 (right panel), the bias-correction actually worsens the forecast at the surface depth at after 15 days into the future. Finally, at day 171 (middle panel), forecasts at surface and 5m depths are generally improved by the bias-correction. Though we only have about 2.5 total years of training data, these plots demonstrate that predicted bias applied to out-of-sample forecasts from GPBC mainly improves forecasts, although there are periods during the year when bias-correction over- or under-corrects or is of the wrong magnitude.

6. Discussion. We introduced an innovative method for forecasting lake temperature profiles 1 to 30 days into the future, bias correcting and surrogate modeling a computer simulation campaign using a lake ecosystem model, GLM. Our framework is thrifty in spite of massive data and cubic bottlenecks, enables iterative forecasting, accounts for input-dependent variance. When compared to other methods, without all of these ingredients, forecasts produced by our bias-corrected Gaussian process surrogate (GPBC) are typically more accurate and deliver superior uncertainty quantification (UQ), especially for forecasts up to two weeks ahead. However, climatological forecasts remain more accurate for predictions beyond two weeks, and in our future work we intend to explore possible reasons for this.

We suspect the main reason we lose to the climatological model (GPO) is a paucity of training data for estimating bias and the quality of NOAA forecasts used to drive GLM. We only have 2.5 years, meaning that we've seen fewer than three examples of yearly variation. Although GPO has access to the same amount of observational data, its simpler design

– not requiring the correction of poor model-based forecasts at longer horizons – helps to prevent over-fitting. Moreover, because the variability of GLM ensemble forecasts increases with forecast horizon, it is likely that the shape and degree of bias at longer horizons is more difficult to estimate compared to shorter horizons, where ensemble forecasts are more in agreement. Thus, bias correction at longer horizons may be less effective than at lower horizons without many more examples of yearly variation.

The quality of NOAA-GLM forecasts is largely dependent on the quality of NOAA forecasts themselves (assuming that GLM is well-calibrated). Weather forecast accuracy more than 10 days into the future declines quickly (Bauer, Thorpe and Brunet, 2015). Moreover, NOAA forecasted variables represent spatial averages over a 25km grid cell, much bigger than FCR for example, which may be too coarse to capture fine-scale variation in meteorological variables. Downscaling and bias-correction of NOAA forecasted variables could result in more accurate lake temperature forecasts from GLM, but additional post-processing of NOAA forecasts would take substantial computation time. Consequently, we decided that and investigation was beyond the scope of our current study. While forecasts of the climatological benchmark model were more accurate than GPBC at longer horizons, the UQ of those forecasts were generally poorer compared to those of GPBC.

Another way to extend this work would be to use GPBC as a likelihood for setting configuration parameters to GLM. In other words, to use the surrogate as a statistical calibration mechanism for the computer model (Kennedy and O’Hagan, 2001; Liu et al., 2009), as opposed to relying on expert opinion using observed meteorological data, not NOAA forecasts. We could also treat the derived input $\phi(t, \lambda)$, allowing us to distinguish forecasts among years, (i.e., the weather inputs) as a latent variable that could be estimated along with other quantities, thus allowing us to distinguish forecasts among years. Such an approach, which involves estimating a high-dimensional free quantity for all t and λ , is precluded, at the moment, by a paucity of sensor measurements. Perhaps once we have accumulated 10+ years of additional data, spanning more yearly environmental variability, the benefits of such an approach might outweigh the additional estimation risk it implies.

Acknowledgments. We thank the Virginia Tech Center for Ecosystem Forecasting team, who provided helpful feedback on this project. Members of the Center, Freya Olsson and Mary Lofton, edited earlier versions of this manuscript. We would also like to thank the Reservoir Group team who provided the lake temperature data analyzed in this study (data are available in the Environmental Data Initiative repository at <https://doi.org/10.6073/pasta/7541e8d297850be7c613d116156735a9>).

Funding. This project was supported by U.S. National Science Foundation grants DBI-1933016, EF-2318861, and DEB-2327030.

REFERENCES

- ANKENMAN, B., NELSON, B. L. and STAUM, J. (2008). Stochastic kriging for simulation metamodeling. In *2008 Winter Simulation Conference* 362–370. IEEE.
- BAKER, E., BARBILLON, P., FADIKAR, A., GRAMACY, R. B., HERBEI, R., HIGDON, D., HUANG, J., JOHNSON, L. R., MA, P., MONDAL, A. et al. (2022). Analyzing stochastic computer models: A review with opportunities. *Statistical Science* **37** 64–89.
- BANERJEE, S., CARLIN, B. P. and GELFAND, A. E. (2003). *Hierarchical modeling and analysis for spatial data*. Chapman and Hall/CRC.
- BANERJEE, S., GELFAND, A. E., FINLEY, A. O. and SANG, H. (2008). Gaussian predictive process models for large spatial data sets. *Journal of the Royal Statistical Society: Series B (Statistical Methodology)* **70** 825–848.
- BAUER, P., THORPE, A. and BRUNET, G. (2015). The quiet revolution of numerical weather prediction. *Nature* **525** 47–55.

- BINOIS, M., GRAMACY, R. B. and LUDKOVSKI, M. (2018). Practical heteroscedastic gaussian process modeling for large simulation experiments. *Journal of Computational and Graphical Statistics* **27** 808–821.
- BINOIS, M. and GRAMACY, R. B. (2021). hetgp: Heteroskedastic Gaussian process modeling and sequential design in R. *Journal of Statistical Software* **98** 1–44.
- BRYNJARSDÓTTIR, J. and O’HAGAN, A. (2014). Learning about physical parameters: The importance of model discrepancy. *Inverse problems* **30** 114007.
- BUECHE, T., HAMILTON, D. P. and VETTER, M. (2017). Using the General Lake Model (GLM) to simulate water temperatures and ice cover of a medium-sized lake: a case study of Lake Ammersee, Germany. *Environmental Earth Sciences* **76** 1–14.
- CAREY, C. C., IBELINGS, B. W., HOFFMANN, E. P., HAMILTON, D. P. and BROOKES, J. D. (2012). Eco-physiological adaptations that favour freshwater cyanobacteria in a changing climate. *Water research* **46** 1394–1407.
- CAREY, C. C., WOELMER, W. M., LOFTON, M. E., FIGUEIREDO, R. J., BOOKOUT, B. J., CORRIGAN, R. S., DANESHMAND, V., HOUNSHELL, A. G., HOWARD, D. W., LEWIS, A. S. et al. (2022). Advancing lake and reservoir water quality management with near-term, iterative ecological forecasting. *Inland Waters* **12** 107–120.
- CHO, K. H., PACHEPSKY, Y., LIGARAY, M., KWON, Y. and KIM, K. H. (2020). Data assimilation in surface water quality modeling: A review. *Water Research* **186** 116307.
- CHRISTIANSON, K. R., JOHNSON, B. M. and HOOTEN, M. B. (2020). Compound effects of water clarity, inflow, wind and climate warming on mountain lake thermal regimes. *Aquatic Sciences* **82** 1–17.
- COLE, T. M. and WELLS, S. A. (2021). CE-QUAL-W2: A two-dimensional, laterally averaged, hydrodynamic and water quality model, version 4.5 Technical Report, Portland State University.
- CRESSIE, N. and JOHANNESON, G. (2008). Fixed rank kriging for very large spatial data sets. *Journal of the Royal Statistical Society: Series B (Statistical Methodology)* **70** 209–226.
- CUDDINGTON, K., FORTIN, M.-J., GERBER, L., HASTINGS, A., LIEBHOLD, A., O’CONNOR, M. and RAY, C. (2013). Process-based models are required to manage ecological systems in a changing world. *Ecosphere* **4** 1–12.
- DATTA, A., BANERJEE, S., FINLEY, A. O. and GELFAND, A. E. (2016). Hierarchical nearest-neighbor Gaussian process models for large geostatistical datasets. *Journal of the American Statistical Association* **111** 800–812.
- DIETZE, M. C., FOX, A., BECK-JOHNSON, L. M., BETANCOURT, J. L., HOOTEN, M. B., JARNEVICH, C. S., KEITT, T. H., KENNEY, M. A., LANEY, C. M., LARSEN, L. G. et al. (2018). Iterative near-term ecological forecasting: Needs, opportunities, and challenges. *Proceedings of the National Academy of Sciences* **115** 1424–1432.
- EMERY, X. (2009). The kriging update equations and their application to the selection of neighboring data. *Computational Geosciences* **13** 269–280.
- FARFÁN, J. F. and CEA, L. (2021). Coupling artificial neural networks with the artificial bee colony algorithm for global calibration of hydrological models. *Neural Computing and Applications* **33** 8479–8494.
- FENOCCHI, A., ROGORA, M., SIBILLA, S., CIAMPITIELLO, M. and DRESTI, C. (2018). Forecasting the evolution in the mixing regime of a deep subalpine lake under climate change scenarios through numerical modelling (Lake Maggiore, Northern Italy/Southern Switzerland). *Climate Dynamics* **51** 3521–3536.
- FER, I., KELLY, R., MOORCROFT, P. R., RICHARDSON, A. D., COWDERY, E. M. and DIETZE, M. C. (2018). Linking big models to big data: efficient ecosystem model calibration through Bayesian model emulation. *Biogeosciences* **15** 5801–5830.
- FRIEDMAN, J. H. (1991). Multivariate adaptive regression splines. *The annals of statistics* **19** 1–67.
- GAL, G., YAEL, G., NOAM, S., MOSHE, E. and SCHLABING, D. (2020). Ensemble modeling of the impact of climate warming and increased frequency of extreme climatic events on the thermal characteristics of a sub-tropical lake. *Water* **12** 1982.
- GNEITING, T. (2002). Compactly supported correlation functions. *Journal of Multivariate Analysis* **83** 493–508.
- GNEITING, T., BALABDAOUI, F. and RAFTERY, A. E. (2007). Probabilistic forecasts, calibration and sharpness. *Journal of the Royal Statistical Society Series B: Statistical Methodology* **69** 243–268.
- GNEITING, T. and RAFTERY, A. E. (2007). Strictly proper scoring rules, prediction, and estimation. *Journal of the American statistical Association* **102** 359–378.
- GOLDBERG, P., WILLIAMS, C. and BISHOP, C. (1997). Regression with input-dependent noise: A Gaussian process treatment. *Advances in neural information processing systems* **10**.
- GRAMACY, R. B. (2016). laGP: large-scale spatial modeling via local approximate Gaussian processes in R. *Journal of Statistical Software* **72** 1–46.
- GRAMACY, R. B. (2020). *Surrogates: Gaussian process modeling, design, and optimization for the applied sciences*. Chapman and Hall/CRC.
- GUINNESS, J. (2018). Permutation and grouping methods for sharpening Gaussian process approximations. *Technometrics* **60** 415–429.

- GUINNESS, J. (2021). Gaussian process learning via Fisher scoring of Vecchia's approximation. *Statistics and Computing* **31** 25.
- HAMILL, T. M., WHITAKER, J. S., SHLYAEVA, A., BATES, G., FREDRICK, S., PEGION, P., SINISKY, E., ZHU, Y., TALLAPRAGADA, V., GUAN, H. et al. (2022). The Reanalysis for the Global Ensemble Forecast System, Version 12. *Monthly Weather Review* **150** 59–79.
- HEATON, M. J., DATTA, A., FINLEY, A. O., FURRER, R., GUINNESS, J., GUHANIYOGI, R., GERBER, F., GRAMACY, R. B., HAMMERLING, D., KATZFUSS, M. et al. (2019). A case study competition among methods for analyzing large spatial data. *Journal of Agricultural, Biological and Environmental Statistics* **24** 398–425.
- HENSMAN, J., FUSI, N. and LAWRENCE, N. D. (2013). Gaussian processes for big data. *arXiv preprint arXiv:1309.6835*.
- HIPSEY, M. R., HAMILTON, D. P., HANSON, P. C., BROOKES, J. D., TROLLE, D. and BRUCE, L. C. (2012). *Blueprint for a unifying framework for synthesis of aquatic ecodynamics*. Brigham Young University.
- HIPSEY, M. R., BRUCE, L. C., BOON, C., BUSCH, B., CAREY, C. C., HAMILTON, D. P., HANSON, P. C., READ, J. S., DE SOUSA, E., WEBER, M. et al. (2019). A General Lake Model (GLM 3.0) for linking with high-frequency sensor data from the Global Lake Ecological Observatory Network (GLEON). *Geoscientific Model Development* **12** 473–523.
- HUANG, L., WANG, J., ZHU, L., JU, J. and DAUT, G. (2017). The warming of large lakes on the Tibetan Plateau: Evidence from a lake model simulation of Nam Co, China, during 1979–2012. *Journal of Geophysical Research: Atmospheres* **122** 13–095.
- JANSE, J., ALDENBERG, T. and KRAMER, P. (1992). A mathematical model of the phosphorus cycle in Lake Loosdrecht and simulation of additional measures. *Hydrobiologia* **233** 119–136.
- JOHNSON, L. R., GRAMACY, R. B., COHEN, J., MORDECAI, E., MURDOCK, C., ROHR, J., RYAN, S. J., STEWART-IBARRA, A. M. and WEIKEL, D. (2018). Phenomenological forecasting of disease incidence using heteroskedastic Gaussian processes: A dengue case study. *The Annals of Applied Statistics* **12** 27–66.
- JONES, D. R. (2001). A taxonomy of global optimization methods based on response surfaces. *Journal of global optimization* **21** 345–383.
- KATZFUSS, M. and GUINNESS, J. (2021). A general framework for Vecchia approximations of Gaussian processes. *Statistical Science* **36** 124–141.
- KATZFUSS, M., GUINNESS, J. and LAWRENCE, E. (2022). Scaled Vecchia approximation for fast computer-model emulation. *SIAM/ASA Journal on Uncertainty Quantification* **10** 537–554.
- KATZFUSS, M., GUINNESS, J., GONG, W. and ZILBER, D. (2020). Vecchia approximations of Gaussian-process predictions. *Journal of Agricultural, Biological and Environmental Statistics* **25** 383–414.
- KAUFMAN, C. G., BINGHAM, D., HABIB, S., HEITMANN, K. and FRIEMAN, J. A. (2011). Efficient emulators of computer experiments using compactly supported correlation functions, with an application to cosmology. *Annals of Applied Statistics* **5** 2470–2492.
- KENNEDY, M. C. and O'HAGAN, A. (2001). Bayesian calibration of computer models. *Journal of the Royal Statistical Society: Series B (Statistical Methodology)* **63** 425–464.
- LADWIG, R., FURUSATO, E., KIRILLIN, G., HINKELMANN, R. and HUPFER, M. (2018). Climate change demands adaptive management of urban lakes: Model-based assessment of management scenarios for Lake Tegel (Berlin, Germany). *Water* **10** 186.
- LADWIG, R., HANSON, P. C., DUGAN, H. A., CAREY, C. C., ZHANG, Y., SHU, L., DUFFY, C. J. and COBOURN, K. M. (2021). Lake thermal structure drives interannual variability in summer anoxia dynamics in a eutrophic lake over 37 years. *Hydrology and Earth System Sciences* **25** 1009–1032.
- LÁZARO-GREDILLA, M. and TITSIAS, M. K. (2011). Variational Heteroscedastic Gaussian Process Regression. In *ICML* 841–848.
- LEON, L. F., SMITH, R. E., ROMERO, J. R. and HECKY, R. E. (2006). *Lake Erie hypoxia simulations with ELCOM-CAEDYM*. Brigham Young University.
- LIU, F., BAYARRI, M., BERGER, J. et al. (2009). Modularization in Bayesian analysis, with emphasis on analysis of computer models. *Bayesian Analysis* **4** 119–150.
- LIU, K., LI, Y., HU, X., LUCU, M. and WIDANAGE, W. D. (2019). Gaussian process regression with automatic relevance determination kernel for calendar aging prediction of lithium-ion batteries. *IEEE Transactions on Industrial Informatics* **16** 3767–3777.
- LOFTON, M. E., HOWARD, D. W., THOMAS, R. Q. and CAREY, C. C. (2023). Progress and opportunities in advancing near-term forecasting of freshwater quality. *Global Change Biology* **29** 1691–1714.
- MOOIJ, W. M., TROLLE, D., JEPPESEN, E., ARHONDITSIS, G., BELOLIPETSKY, P. V., CHITAMWEBWA, D. B., DEGERMENDZHY, A. G., DEANGELIS, D. L., DE SENERPONT DOMIS, L. N., DOWNING, A. S. et al. (2010). Challenges and opportunities for integrating lake ecosystem modelling approaches. *Aquatic Ecology* **44** 633–667.
- OAKLEY, J. E. and O'HAGAN, A. (2004). Probabilistic sensitivity analysis of complex models: a Bayesian approach. *Journal of the Royal Statistical Society Series B: Statistical Methodology* **66** 751–769.

- QUADRIANTO, N., KERSTING, K., REID, M. D., CAETANO, T. S. and BUNTINE, W. L. (2009). Kernel conditional quantile estimation via reduction revisited. In *2009 Ninth IEEE International Conference on Data Mining* 938–943. IEEE.
- QUINONERO-CANDELA, J. and RASMUSSEN, C. E. (2005). A unifying view of sparse approximate Gaussian process regression. *The Journal of Machine Learning Research* **6** 1939–1959.
- RAZAVI, S., TOLSON, B. A. and BURN, D. H. (2012). Review of surrogate modeling in water resources. *Water Resources Research* **48**.
- ROY, P. T., EL MOÇAYD, N., RICCI, S., JOUHAUD, J.-C., GOUTAL, N., DE LOZZO, M. and ROCHOUX, M. C. (2018). Comparison of polynomial chaos and Gaussian process surrogates for uncertainty quantification and correlation estimation of spatially distributed open-channel steady flows. *Stochastic environmental research and risk assessment* **32** 1723–1741.
- SANTNER, T. J., WILLIAMS, B. J., NOTZ, W. I. and WILLIAMS, B. J. (2018). *The design and analysis of computer experiments* **2**. Springer.
- SAUER, A., COOPER, A. and GRAMACY, R. B. (2023). Vecchia-approximated deep Gaussian processes for computer experiments. *Journal of Computational and Graphical Statistics* **32** 824–837.
- SHIKHANI, M., MI, C., GEVORGYAN, A., GEVORGYAN, G., MISAKYAN, A., AZIZYAN, L., BARFUS, K., SCHULZE, M., SHATWELL, T. and RINKE, K. (2022). Simulating thermal dynamics of the largest lake in the Caucasus region: The mountain Lake Sevan. *Journal of Limnology* **81**.
- STEIN, M. L., CHI, Z. and WELTY, L. J. (2004). Approximating likelihoods for large spatial data sets. *Journal of the Royal Statistical Society: Series B (Statistical Methodology)* **66** 275–296.
- STROUD, J. R., STEIN, M. L. and LYSÉN, S. (2017). Bayesian and maximum likelihood estimation for Gaussian processes on an incomplete lattice. *Journal of computational and Graphical Statistics* **26** 108–120.
- THOMAS, R. Q., FIGUEIREDO, R. J., DANESHMAND, V., BOOKOUT, B. J., PUCKETT, L. K. and CAREY, C. C. (2020). A near-term iterative forecasting system successfully predicts reservoir hydrodynamics and partitions uncertainty in real time. *Water Resources Research* **56** e2019WR026138.
- THOMAS, R. Q., MCCLURE, R. P., MOORE, T. N., WOELMER, W. M., BOETTIGER, C., FIGUEIREDO, R. J., HENSLEY, R. T. and CAREY, C. C. (2023). Near-term forecasts of NEON lakes reveal gradients of environmental predictability across the US. *Frontiers in Ecology and the Environment* **21** 220–226.
- VECCHIA, A. V. (1988). Estimation and model identification for continuous spatial processes. *Journal of the Royal Statistical Society: Series B (Methodological)* **50** 297–312.
- WARD, N. K., STEELE, B. G., WEATHERS, K. C., COTTINGHAM, K. L., EWING, H. A., HANSON, P. C. and CAREY, C. C. (2020). Differential responses of maximum versus median chlorophyll-a to air temperature and nutrient loads in an oligotrophic lake over 31 years. *Water Resources Research* **56** e2020WR027296.
- WETZEL, R. G. (2001). *Limnology: lake and river ecosystems*. gulf professional publishing.
- WILLIAMS, C. K. and RASMUSSEN, C. E. (2006). *Gaussian processes for machine learning* **2**. MIT press Cambridge, MA.
- WU, L., PLEISS, G. and CUNNINGHAM, J. P. (2022). Variational nearest neighbor Gaussian process. In *International Conference on Machine Learning* 24114–24130. PMLR.
- YANG, J., JAKEMAN, A., FANG, G. and CHEN, X. (2018). Uncertainty analysis of a semi-distributed hydrologic model based on a Gaussian Process emulator. *Environmental Modelling & Software* **101** 289–300.
- ZHANG, J. and KATZFUSS, M. (2022). Multi-scale Vecchia approximations of Gaussian processes. *Journal of Agricultural, Biological and Environmental Statistics* **27** 440–460.

APPENDIX A: TOY PROBLEM

This 1d example was introduced by [Binois, Gramacy and Ludkovski \(2018\)](#). The mean function is $f(x) = 2 \times \exp(-30(x - 0.25)^2 + \sin(\pi x^2)) - 2$ with a noise function of $r(x) = \frac{1}{3} \exp(\sin(2\pi x))$. Observations are simulated as $y \sim f(x) + \epsilon$, where $\epsilon \sim N(0, \sigma^2 = r(x))$. The training data comprise of 100 input locations equally spaced in $[0, 1]$, with 15 replicates observed upon each. Therefore, the total number of observations is $N = 15 \times 100 = 1500$. The simulated data can be represented as $D_N = (x_i, y_i), i = 1 \dots N$. Let \mathbf{X}_N and \mathbf{Y}_N collect inputs and outputs, respectively. We then model D_N as $\mathcal{GP}(D_N)$ and use four fitted modes:

1. a full heteroscedastic GP fit from the `hetGP` R package ([Binois and Gramacy, 2021](#)), via `mleHetGP` as in Section 5.1;
2. a moments-based alternative using a full GP fit via the `laGP` R package ([Gramacy, 2016](#));

3. moments-based alternatives using our Vecchia method (Sections 3.2 and 3.3) with a) the predictive mean $\mu_n^{(v)}$ (Vecchia A) and b) the upper 95th quantile of the predictive mean $\mu_n^{(v)95}$ resulting from the second-moments fit, $\mathcal{GP}(D_n^{(v)})$, from Section 3.3 (Vecchia B).

The implementation of 2) was identical to Vecchia A, but the GPs fitted to first and second moments were full GP fits rather than Vecchia approximations, and models were fitted using the Gaussian covariance kernel. Joint inference for lengthscale and nugget parameters were conducted with `jmlGP`.

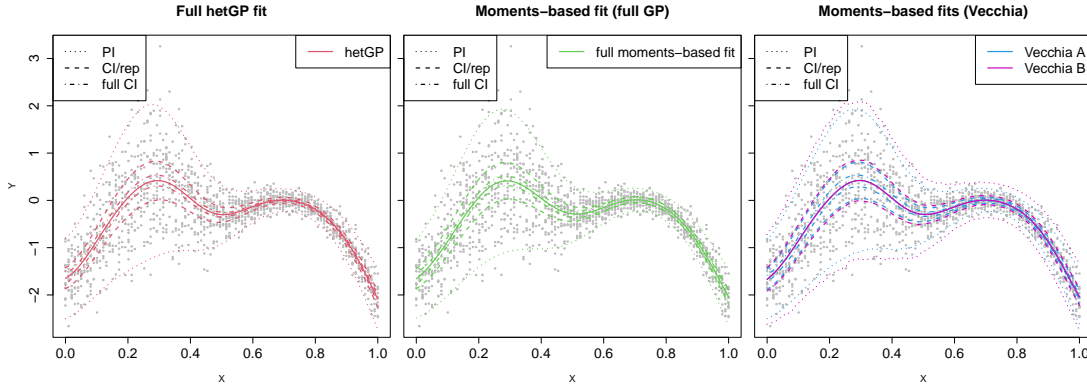


FIG 17. Fits for the four methods used in the toy example: *hetGP* (left), a moments-based alternative via a full GP fit (center), and moments-based alternatives using Vecchia (right). Vecchia A and B are as described above. 95% PI, CI, and “full CI” coverages are represented by dotted, dashed, and dot-dashed lines, respectively.

	PI	CI	CI-full
hetGP	0.94	0.97	1.00
Full moments-based fit	0.93	0.94	0.95
Vecchia A	0.94	0.96	0.98
Vecchia B	0.98	1.00	1.00

TABLE 1

95% PIs and CIs for the four methods used in the toy example.

Simulated observations (gray dots), along with fits from all four models are shown in Figure 17, and 95% PIs and CIs are shown in Table 1. The predictive means from all four methods are nearly identical. We calculated CI coverage for methods 1-3 above in two ways. For moments-based methods 2 and 3 we calculated standard errors for CI/PI calculations using $\hat{\sigma}_n^{\text{SK}}(\mathbf{x})^2$ from Eq. 12. For the *hetGP* implementation, our calculations were similar but involved dividing the diagonal of the predictive covariance matrix plus a varying nugget term by the number of replicates (15). We then determined the percentage of sample means that fell within CIs. To calculate PIs we did not divide by the number of replicates and report the percentage of data points that fell within the intervals. For this CI/PI calculation, performance is similar among the four methods with Vecchia B providing more conservative UQ by design. Vecchia B achieved 98% and 100% PI and CI coverage, respectively, while coverages of the other three methods ranged between 93 and 97% (Table 1, middle column).

However, this approach constitutes a CI for the average based on an iid assumption, which for this toy problem, is not true. When the spatial nature of the model is taken into account, the CIs become much narrower. When accounting for the spatial nature of the model in the toy problem, CIs should be compared to the *true mean*, not the sample average. For a real-world problem, we do not know the true mean, but because we know it in this example, it

is possible to assess coverage in this way also. The standard error (SE) for these coverage calculations for methods 2) and 3) are given in Eq. (15):

$$(15) \quad \text{SE} = \sqrt{\frac{\mu_n^{(v)*}(\mathbf{x})}{\text{dof}} + \frac{\sigma_n^{2(m)}(\mathbf{x})}{\text{dof}}}, \quad \text{where} \quad \text{dof} = \min_{i=1, \dots, n} \sum_{j=1}^n \Sigma(\bar{\mathbf{X}}_n)_{ij}$$

Here, $\Sigma_{ij} = k(q(\mathbf{x}_i, \mathbf{x}_j)) + g\mathbb{I}_{\{i=j\}}$, $k(\cdot)$ is the Gaussian covariance kernel, and $\Sigma(\bar{\mathbf{X}}_n)$ is $n \times n$, where $\bar{\mathbf{X}}_n$ is the matrix of unique input locations as defined in Section 3.2. In Eq. (15), the quantity $\mu_n^{(v)*}(\mathbf{x})$ is derived from the *full* GP fit to $D_n^{(v)} = (\bar{\mathbf{X}}_n, \bar{\mathbf{S}}_n)$ via `jmlGP` from the `laGP` package. The quantity $\sigma_n^{2(m)}(\mathbf{x})$ either represents the predictive variance of the full GP fit to $D_n^{(m)} = (\bar{\mathbf{X}}_n, \bar{\mathbf{Y}}_n)$ (the moments-based approach method 2) or predictive variance of the Vecchia-approximated fit to $D_n^{(m)}$ (moments-based approaches Vecchia A and B in method 3). While the SE in Eq. (15) is partially based on a full GP fit using a Gaussian covariance kernel, coverages for Vecchia A and B (which are fitted using a Matern kernel with a smoothness parameter of 3.5) calculated this way still represent good estimates for the purposes of this example. Calculating true confidence intervals with the heteroscedastic GP implementation in method 1) requires only the diagonal of the “no nugget” predictive variance, which is returned by `mleHetGP`.

The final step involves an MCMC experiment in which CI coverages are calculated 100 times using Eqn. (15), and the proportion of times the true mean falls within the CI is reported. These coverage values are given in the right-most column of Table 1. All four methods perform well in this regard, with all achieving at least 97% coverage.